JGR Solid Earth

RESEARCH ARTICLE
10.1029/2022JB025209

A Discrete Elements Study of the Frictional Behavior of Fault Gouges

E. Papachristos[1], I. Stefanou[1], and J. Sulem[2]

[1]Nantes Université, Ecole Centrale Nantes, CNRS, Institut de Recherche en Génie Civil et Mécanique (GeM), UMR 6183, Nantes, France, [2]Laboratoire Navier, Ecole des Ponts ParisTech, CNRS UMR 8205, Université Gustave Eiffel, Marne-la-Vallée, France

Key Points:

- The local stick-slip motion vanishes for multiple, averaged tests and does not affect the expected value of the apparent frictional response
- Both the thickness of the principal slip zone and the critical slip distance scale with the mean particle diameter
- Particle size distribution and shearing velocity exerts a second order control on global friction

Correspondence to:

I. Stefanou,
ioannis.stefanou@ec-nantes.fr

Citation:

Papachristos, E., Stefanou, I., & Sulem, J. (2023). A discrete elements study of the frictional behavior of fault gouges. *Journal of Geophysical Research: Solid Earth*, *128*, e2022JB025209. https://doi.org/10.1029/2022JB025209

Received 20 JUL 2022
Accepted 3 DEC 2022

Author Contributions:

Conceptualization: E. Papachristos, I. Stefanou, J. Sulem
Formal analysis: E. Papachristos, I. Stefanou, J. Sulem
Funding acquisition: I. Stefanou
Investigation: E. Papachristos, I. Stefanou, J. Sulem
Methodology: E. Papachristos, I. Stefanou, J. Sulem
Project Administration: I. Stefanou
Software: E. Papachristos
Supervision: I. Stefanou, J. Sulem
Validation: E. Papachristos, I. Stefanou, J. Sulem
Visualization: E. Papachristos
Writing – original draft: E. Papachristos
Writing – review & editing: E. Papachristos, I. Stefanou, J. Sulem

Abstract A series of discrete elements simulations is presented for the study of fault gouges' frictional response. The gouge is considered to have previously undergone ultra-cataclastic flow and long-time consolidation loading. We explore the effect of different particle characteristics such as size, polydispersity, and also shearing velocities on gouge's response under the conditions met in the seismogenic zone. Monte-Carlo analyses suggest that the local stick-slip events disappear when averaging over a large number of numerical samples. Moreover, the apparent material frictional response remains almost unaffected by the spatial randomness of particles' position and by the particle's size distribution. On the contrary, the mean particle size controls the formation and thickness of the observed shear bands, which appear after the peak friction is met. Furthermore, the apparent friction evolution fits well to an exponential decay law with slip, which involves a particle size dependent critical slip distance. For the studied conditions and depth, the shearing velocity is found to play a secondary role on the apparent frictional response of the gouge, which highlights the importance of analyses involving multiphysics for studying the rheology of fault gouges. Besides improving the understanding of the underlying physics of the problem, the above findings are also useful for deriving pertinent constitutive models in the case of modeling with continuum theories.

Plain Language Summary Understanding the response of a fault gouge, the granular material at the core of fault zones, can shed light on the way earthquakes are nucleated. For this purpose, in this paper, a series of particle-based simulations of a fault gouge, under conditions similar to the ones expected at deep down at the seismogenic zone, are conducted. A full-scale fault with dimensions of the order of kilometers is almost impossible to be simulated at the grain-scale. In order to capture the inhomogeneities at this level, the response of several, small samples is combined in a stochastic-ensemble manner. The results suggest that local stick-slip events are vanishing with increasing number of tests thus, they are not critical for the macroscopic, global, material's response. Contrary to this, the amount of slip needed to promote earthquake instabilities is shown to vary with respect to the mean particle size of the material. Finally, the granular polydispersity and the slip velocity do not seem to affect the system's behavior. The later highlights possible important role of multiphysics on the rheology of fault gouges and provides evidence for the constitutive assumptions used in continuum models.

1. Introduction

The crustal deformation is localized at fault zones, which enclose a volume that spans from tens to several thousands of cubic kilometers. However, most of the deformation is accommodated at the very center of the fault zone, a thin region, few millimeters wide, the fault core. Repeated slip events cause wearing of the adjacent rock walls (due asperities breakage or plowing) and filling of the fault core with brittle wear products. In a second step, they cause further mineral fragmentation due to cataclastic flow (Davidesko et al., 2014; Lyakhovsky & Ben-Zion, 2014; Lyakhovsky et al., 1997; C. G. Sammis & Ben-Zion, 2008; Scholz, 2002; W. Wang & Scholz, 1994). The resulting complex granular material is termed fault gouge. Given the process of formation of the fault gouge (wear and breakage), particles' shape is angular, and their size distribution is typically wide (Marone & Scholz, 1989; C. G. Sammis et al., 1986). During slip, a secondary strain localization zone (shear band) may form inside the granular gouge layer, which will control the softening branch of the slip response of the granular layer (Mühlhaus & Vardoulakis, 1987; J. R. Rice, 1976; Rudnicki & Rice, 1975, among others). This zone is referred to as the principle slip zone (PSZ; Ben-Zion & Sammis, 2003; Platt et al., 2014). Consequently, the frictional behavior of the fault gouge, plays a key role for the response of the fault zone during slip. In this

work, we consider mature faults' gouge, which are healed after long periods of straining that lead to strengthening and new seismic events due to softening/weakening during slips.

A lot of effort has been put over the last decades to explore the constitutive behavior of fault gouges. These works are mainly experimental (Anthony & Marone, 2005; Chambon et al., 2002; Collettini et al., 2009; Dieterich & Carter, 1981; Mair et al., 2002; Mair & Marone, 1999; Marone et al., 1990; Marone & Scholz, 1989; Ruina, 1983; Scholz, 2002; Scuderi & Collettini, 2016) and give valuable information about the thermo-chemo-hydro-mechanical behavior of gouges. The most frequently used constitutive law for friction is the Rate-and-State friction law (see Dieterich, 1978; Dieterich & Carter, 1981), which successfully fits a large spectrum of experimental results. In this model, the friction depends on the slip rate (velocity-dependent), a state variable, whose physical meaning can be related to various underlying physical processes (e.g., Aharonov & Scholz, 2018), and a characteristic length, D_c, which determines the post peak softening. The aforementioned length scale is a function of the particles' size for faults with gouge (Dieterich & Carter, 1981).

The consideration of the particles' size and its effect on the frictional response of the fault gouge is intrinsic in detailed numerical simulations using the Discrete Element Method (DEM). DEM is employed in the literature for investigating the mechanical response of idealized fault gouges (Abe et al., 2002; Abe & Mair, 2009; Aharonov & Sparks, 1999, 2002; Ferdowsi & Rubin, 2020; Guo & Morgan, 2004, 2006, 2007; Hazzard & Mair, 2003; Mair & Abe, 2008; Morgan, 1999; Morgan & Boettcher, 1999) and granular materials more generally (Azéma et al., 2012; Estrada et al., 2008; Nguyen et al., 2015). However, these works focus mainly on the appearance of repeating, abrupt, local stick-and-slip phenomena due to grain force chains changes (formation and collapse) and less on the constitutive frictional behavior of the granular gouge. They consider these events as the dominant, instability factor in seismic fault cores.

In the present article, we consider the medium's disorder through a statistical ensemble approach. This allows us to take into account the disorder of the medium in a statistical sense. More specifically, a volume of the fault core is simulated by a series of N DEM tests, with random packing of particles, each one representing a Stochastic Elementary Volume (SEV) of the fault core. The global response of the fault is thus represented by the statistical average of the N responses of the DEM models. By calculating the expected value of different parameters regarding the apparent frictional response and deformation of the system, we derive useful conclusions concerning: (a) the statistically vanishing local stick-and-slip events with increasing number of tests, (b) the scaling of the critical slip distance, D_c, with the mean particle size, d_{50}, (c) the formation of a localized zone (shear band) of shear deformation whose thickness scales with d_{50} independently of the particle size distribution (PSD) and (d) the absence of significant velocity-weakening behavior at the confinement stress level tested and for the parameters used.

Our DEM analyses involve a granular fault gouge at seismogenic depth which has undergone a severe and long-time cataclasis before the slip takes place, leading to a highly interlocked granular material. The behavior of this material is expected to show a different behavior than compacted, non-interlocked glass-beads analogs that are often used in laboratory experiments or in DEM simulations. It is worth noting that our numerical model is an idealization of a real fault gouge. Nevertheless, it allows to draw qualitative results showing the effect of grain size related to the stochastic apparent frictional behavior of the system. Moreover, our DEM analyses allow to access information that are hard, if not impossible, to obtain from real experiments.

Particular care was taken to use adequate scalings in order to accelerate calculations as much as possible without altering the physics of the problem. This is a central issue given the stochastic approach of this work, which involves tens of analyses in order to assure a correct statistical interpretation of the results and show a Monte-Carlo based $1/\sqrt{N}$ convergence. Furthermore, the scales controlling the apparent frictional behavior have been identified by spectral decomposition of the frictional response and the related slip events. This analysis has shown that results of single tests might be misleading. The high-frequency events related to grain-scale vanish as soon as the response of several tests is averaged. Then the global material response governs the frictional behavior of the fault gouge. Physically, this averaged response can be explained as the overall response not only of a thin slice of gouge material, but of a larger volume (see Figure 1).

Grain crushing is indirectly addressed in the present work. More precisely, having found that the shear band thickness (which would correspond to the size of the principal slip zone, see Section 2.2) and the critical sip distance scale with the mean particle size, makes possible the study of the evolution of the apparent frictional behavior of the gouge layer by decreasing the particle size during shearing. However, we do not study the effects

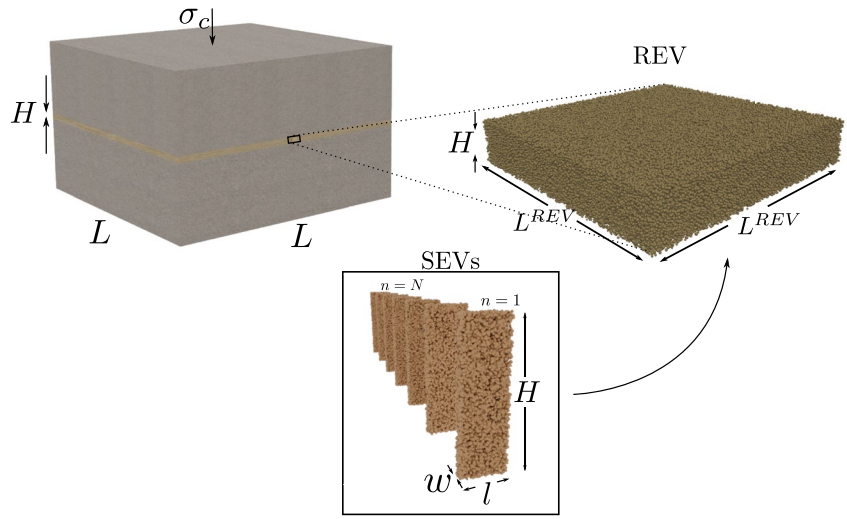

Figure 1. Different length scales inside a fault gouge layer of size $L \times L \times H$. H is the (finite) thickness of the fault core (and consequently the specimen's height). The material behavior of the fault gouge is studied at the level of the Representative Elementary Volume (REV) of lateral size L^{REV} and height H. The REV is approximated by a stochastic ensemble of a series of specimens or Stochastic Elementary Volumes (SEVs) at the level of the microstructure ($l \ll L^{REV} \ll L$, $w \ll L^{REV} \ll L$).

related to powder production and lubrication (Reches & Lockner, 2010), which are thought to be phenomena of a finer scale. From an energetic point of view, it is found that grain-crushing plays minor role in the total dissipated energy and thus is neglected from the problem (see Appendix A).

The findings of this work will lead to a better understanding of the frictional response of seismic fault gouges during slip and as a consequence of earthquake nucleation phenomena. Furthermore, the key-parameters controlling the frictional response and more precise bounds in friction may contribute in controlling seismicity in the future (Papachristos & Stefanou, 2021; Stefanou, 2019; Stefanou & Tzortzopoulos, 2022; Tzortzopoulos et al., 2021).

First, the numerical model used for the micro-mechanical analysis of the fault gouge is explained in Section 2. Then an extensive review of the numerical setup is presented in Section 2.1. More explicitly, it is explained: the way the gouge material analog and boundary conditions are simulated to be representative of realistic fault gouges in seismogenic depth, the separation of the characteristic scales of the problem, and the scaling procedure to obtain an equivalent medium without loosing any information. The stochastic interpretation of the model and the Monte-Carlo error convergence are then explained in Section 3. Once the simulations are setup, the shear band thickness and the critical slip distance is examined in order to obtain quantitative and qualitative descriptors for (a) slip-weakening and (b) velocity weakening behavior in Section 4. Finally, an extended discussion is given in Section 5, highlighting the significance of the findings of this work related to the earthquake instability and to slip.

2. Discrete Elements Gouge Model

2.1. DEM for Gouge Modeling

The analysis in this work is performed in the framework of the DEM. The fault gouge is modeled by spherical discrete element particles. The particles, interact with each other according to the inter-particle constitutive laws of friction and their motion is governed by Newton's second law of motion. The numerical analyses are conducted using the open-source platform YADE-Open DEM (Kozicki & Donzé, 2008; Šmilauer et al., 2015).

To a certain extent, DEM restores the micro-mechanical geometrical complexity of the original problem. Furthermore, it gives access to local micro-mechanical information at the particles' level, which is practically impossible to get through real experiments. Finally, the constitutive behavior of the simulated material emerges naturally throughout the analysis, rather than obeying to imposed ad-hoc behaviors.

Considering a purely frictional (cohesionless) granular medium, the simulated particles interact with each other under normal and tangential forces acting on them. Each particle is assigned with a radius R and a material

described by density ρ and Young's modulus E. We assume a Coulomb friction between particles, with a friction angle ϕ. The studied material, fault gouge, is usually characterized by (a) angular fragments, products of previous ultra-cataclastic flow inside the fault core and (b) a dense structure due to the high effective stresses. These two factors lead to a highly interlocked initial material state. In order to account for particle shape effect in the analysis several alternatives exist for DEM. A computationally efficient method, which is used hereafter, is including rolling and twisting resistance moments on the interactions between grains (see Estrada et al., 2011; Hosn et al., 2017; Iwashita & Oda, 1998; Liu et al., 2018; Plassiard et al., 2009), otherwise the exact grains shape should be taken into account (Kawamoto et al., 2016; Mollon et al., 2020), but this is a computationally very intensive task. For the approach used in this work, four extra micro-mechanical parameters need to be added at the contact level, the rolling stiffness, k_r, the plastic limit for the rolling moment, η_r, the twisting stiffness, k_{tw}, and the plastic limit for the twisting moment, η_{tw}.

Considering two particles A and B with radii R_A and R_B, respectively, in contact, the inter-particle forces are expressed as follows:

$$\begin{aligned}
\vec{F}_n &= k_n \{\delta_n\} \vec{n} \\
\Delta\vec{F}_s &= -k_s \Delta\vec{U}_s, \quad \text{with } \|\vec{F}_s\| \leq \|\vec{F}_n\| \tan(\phi) \\
\Delta\vec{M}_r &= -k_r \Delta\vec{\theta}_r, \quad \text{with } \|\vec{M}_r\| \leq \|\vec{F}_n\| \eta_r \min(R_A, R_B) \\
\Delta\vec{M}_{tw} &= -k_{tw} \Delta\vec{\theta}_{tw}, \quad \text{with } \|\vec{M}_{tw}\| \leq \|\vec{F}_n\| \eta_{tw} \min(R_A, R_B)
\end{aligned} \tag{1}$$

where $\vec{F}_n$, $\vec{F}_s$, $\vec{M}_r$ and $\vec{M}_{tw}$ are respectively the normal force, shear force, rolling moment and twisting moment, k_n, k_s, k_r, k_{tw}, the normal, shear, rolling, and twisting stiffnesses, δ_n the penetration length, $\vec{n}$ the contact normal and $\Delta\vec{U}_s, \Delta\vec{\theta}_r, \Delta\vec{\theta}_{tw}$ are the relative shear displacement, rotation angle and spin angle, respectively. The dependence on particle radii and stresses is a result of Hertzian contact theory of which the set of Equation 1 is a linearization. For more details, we refer to Johnson (1985) and Šmilauer et al. (2015). The normal force $\vec{F}_n$ is zero if particles are not in contact that is when $\delta_n \leq 0$. No inter-particle bonding is considered herein. As a result, no macroscopic, apparent cohesion is observed, as also shown in Figure B2 in Appendix B.

Macroscopic elastic properties remain independent of particle size by defining contact stiffnesses based on a particle stiffness modulus E and dimensionless material parameters (coefficients) of shear, α_s, rolling α_r, and twisting α_{tw} (Hosn et al., 2017; Plassiard et al., 2009) as follows:

$$\begin{aligned}
k_n &= 2E_p \frac{R_A R_B}{R_A + R_B} \\
k_s &= \alpha_s k_n \\
k_r &= \alpha_r R_A R_B k_s \\
k_{tw} &= \alpha_{tw} R_A R_B k_s
\end{aligned} \tag{2}$$

The system is integrated in time explicitly, using a leapfrog, central finite difference approximation algorithm (Šmilauer et al., 2015).

2.2. Original Geophysical Problem

Earthquakes are usually expected to occur inside the limits of the so-called seismogenic zone. This zone refers to depths between 6 and 14 (km) (Saffer & Marone, 2003; Sibson, 2011). Due to tectonic movement, strain is accommodated inside fault cores and on the surrounding rock formations. The cores of mature faults are often composed of granular material that has been produced during abrasive wear of the interface asperities or due to plowing of harder minerals onto softer ones (Scholz, 2002). During pre- and co-seismic slip, shear strain is accommodated in thinner zones called PSZs, which correspond to shear bands formed in the granular gouge material (Mühlhaus & Vardoulakis, 1987; J. R. Rice, 1976; Rudnicki & Rice, 1975, among others).

Earthquake nucleation depends on many factors. A central one is fault friction. At the fault's core, a zone that undergoes a pronounced localized deformation upon far-field tectonic movement is formed. This thin zone opposes the fault interfaces movement through frictional resistance. It is composed of ultracataclastic materials

and has a complex structure (Ben-Zion & Sammis, 2003; Brodie et al., 2007) as a result of the numerous physico-chemical processes that occur during pre- and co-seismic slip (see Anthony & Marone, 2005; Rattez, Stefanou, & Sulem, 2018; Rattez, Stefanou, Sulem, Veveakis, & Poulet, 2018; Reches & Lockner, 2010; Scuderi et al., 2017; Tinti et al., 2016, among others).

The complex composition of this region, results in an apparent friction that does not depend only on the extent of the slip and the slip-rate, but also on phenomena (geometrical, mechanical or physico-chemical) at the level of the microstructure and of the interstitial fluids (see e.g., Brantut & Sulem, 2012; Sulem & Famin, 2009; Veveakis et al., 2010, 2013). However, here we consider only a dry granular medium in our discrete element analysis. As far as it concerns earthquake nucleation, knowing the constitutive behavior of the apparent friction is of paramount importance as it determines the conditions for which the dynamic instability can take place. A dynamic instability can take place when the material is slip-rate weakening or when the slip-weakening is higher than the negative slope of the effective elastic response of the surrounding to the fault rocks, which represents the elastic unloading of the system that cannot be counter balanced by fault friction (Dieterich & Carter, 1981; Gu et al., 1984; J. Rice & Ruina, 1983; Scholz, 2002; Stefanou, 2019). Supposing a piecewise linear friction law, where friction drops from peak value, μ_{peak}, to the residual value, μ_{res}, in a characteristic distance, D_c, the stability condition becomes $\sigma_c(\mu_{res} - \mu_{peak})/D_c > -G/L$ where σ_c is the (Terzaghi) effective normal stress applied to the fault, G is the effective shear elastic modulus of the surrounding to the fault rocks and L the fault's length (see related paragraph in Stefanou, 2019, among others). A similar instability condition holds for "velocity weakening" materials when the rate-and-state friction law is used (see Ruina, 1983; Scholz, 2002, among others).

2.3. Numerical Analog of Fault Gouge During Slip

There is a number of conditions that will be fulfilled in this work, to approach as close as possible to the original problem and to the conditions of a mature fault that has undergone fragmentation (cataclasis), wear, consolidation, and other phenomena related to healing during the long time-scale before a new seismic slip event.

First of all, (a) at such depths, elevated effective stresses at the order of 75–225 (MPa) are expected, depending on the tectonic setting and fluid upflow. Furthermore, (b) the granular gouge inside mature fault cores, is a product of excessive wear from previous slip events which lead to cataclastic flow (Collins-Craft et al., 2020; Numelin et al., 2007; Scholz, 2002). Due to this fragmented nature of the granular core, the in situ stress level, the frequently reported low permeability (see Fairley et al., 2003; Morrow et al., 1984; Takahashi, 2003) and the large time intervals between the seismic slips, the initial state of the gouge layer (at depth) is expected to be dense (of low porosity) and (c) highly interlocked, but cohesion-less (the importance of the initial state of the granular material is further discussed in Appendix B). It is noted that the dilation is negligible as compared to the friction angle of the material, about two orders of magnitude lower (see Appendix B). The degree of interlocking can depend, among others, on the porosity, the grain size distribution, and on the degree of angularity (see Collins-Craft et al., 2020, and references therein). The size of gouge particles usually follows a wide distribution (d), while the upper bound for the mean particle diameter is at the order of 100 (μm) (e) (Morgan, 1999; Saffer & Marone, 2003). The mean size of the particles is also expected to be reduced (f) during the seismic slip, due to grain crushing (Scholz, 2002). Finally, a large range of slip velocities has been observed (g) spanning from 10^{-10} to 1 ($m.s^{-1}$) during seismic slip (Reches & Lockner, 2010).

When the above conditions are met, the emerging fault gouge can be characterized as healed and provide the necessary weakening mechanisms for new seismic slip events to occur. Notice, that this healed granular gouge can present pronounced weakening without being cohesive, as shown in Section 4 and Appendix B.

In order to mimic the conditions described above, a granular DEM packing, is subjected to consolidation (or else, compaction to the in situ stress conditions), and then to direct shear. The following procedure is used in the numerical simulations. A numerical specimen is first created by random deposition of spherical DEM particles. The specimen is periodic along its length and width, while on its top and bottom is bounded by rigid plates. The initial material is assigned with $\phi \simeq 0°$ and no rotational moments, in order to enhance compaction and densification of the packing that will be sheared. It is then isotropically compacted to a dense state. Next, the upper plate is displaced to compact the specimen to consolidate it, up to the point that the desired effective stress level σ_c is achieved and is homogeneous inside the specimen. The final material properties are then assigned to the particles and their existing interactions. This way, the conditions (a)–(c) are met. Once the packing is in equilibrium, the

top and bottom plates are assigned with a constant shear velocity $V_s/2$ in opposite directions. A velocity controlled servomechanism, applied on the top plate, ensures the effective stress to be kept constant during shearing and equal to the desired value.

In this work, we analyze the frictional behavior of the granular gouge material. The 3D DEM model represents an elementary volume enclosed by ($l \times w \times H$) in Figure 1. The model considers a constant shearing velocity of the top and bottom blocks (which are modeled as rigid plates). The specimen used for the tests is in three dimensions, composed of spherical particles and it has a size of $1.8 \times 0.54 \times 6.3$ (mm), which corresponds, in average, to $20 \times 6 \times 70$ mean particle diameters, d_{50}, (length along shearing axis × width of out of plane axis × height or thickness of the layer). Note that although this is a uni-directional shearing test, important 3D effects may arise from particle re-organization, thus the 3D dimension should not be disregarded (Hazzard & Mair, 2003).

The periodicity of the packing ensures invariance along the slip direction and, given the packing's width, it allows local granular density fluctuations and jamming-unjamming transition along the width-axis of the specimen (Dorostkar et al., 2017a; Ferdowsi et al., 2014; Marone et al., 2008). Thus, boundary effects on these axes are avoided. Furthermore, the non-periodic, plate boundaries at top-bottom of the specimen enable the formation of strain localization inside the specimen during shearing. It is worth emphasizing that there are enough particles along the vertical axis for a shear band to form (Rattez, Stefanou, & Sulem, 2018) and avoid boundary effects. Note that the later is not the case in most of the DEM studies on fault gouge shear tests (e.g., Dorostkar et al., 2017a, 2017b; Ferdowsi et al., 2014). Consequently, the apparent shear stress-shear strain relation is influenced (in those works) by the limited height of the specimen. The thickness of the shear band influences directly the above-mentioned relation as mentioned in many works (Needleman, 1988; Rattez, Stefanou, & Sulem, 2018).

The reference scenario in this work will consider a mean particle diameter of $d_{50} = 90$ (μm), which falls inside the limits of condition (e). In order to account for the PSD of condition (d), three different PSDs will be tested: one monodisperse and two with uniform distributions setting $d = d_{50}(1 \pm f)$, where f is a fuzziness index describing the width of the distribution. The f value will be set to $f = 0.5$ and $f = 0.7$, giving, for the case of $d_{50} = 90$ (μm), $d_{\min} = 45$ (μm), $d_{\max} = 135$ (μm) with $d_{\max}/d_{\min} = 3$ and $d_{\min} = 27$ (μm), $d_{\max} = 153$ (μm) with $d_{\max}/d_{\min} = 5$ respectively. Although this is a polydisperse distribution and very close to the (2D) fractal PSD used by Morgan and Boettcher (1999), which is observed in several naturally and experimentally sheared gouges (see Biegel et al., 1989; Blenkinsop, 1991; Hooke & Iverson, 1995; Marone & Scholz, 1989; C. Sammis et al., 1987; C. G. Sammis et al., 1986), it still is far away from a complete, ultracataclastic gouge PSD, which ranges from nanometers to hundreds of micro-meters. The reason for not using such fine distributions is the prohibiting large computational cost of the model (i.e., very low timestep controlled by the small particles and very large total number of particles, see also Section 5). However, our modeling assumption can provide useful insights for the role of PSD width as shown in Section 4.

Excessive grain crushing is expected under the studied conditions. However, it is shown in Appendix A that the energy release from this phenomenon is not expected to vary the results of this study. Thus, grain size reduction is taken into account implicitly, to satisfy condition (f). Three different mean particle sizes, d_{50} are tested, 60, 90, 120 (μm) and their behavior is compared in terms of shear band width and frictional response. Note that the production of fines and the related lubrication phenomena (Reches & Lockner, 2010) are of course not taken into account using the above assumptions, but it lays beyond the scope of the current work.

Apparent rate effects and velocity weakening of the granular layer during slip are studied by using a range of different shearing velocities from 10^{-3} to 1 (m/s). This range falls in the limits of condition (g) and sheds light to the importance of rate effects during weakening in purely mechanical simulations of gouge material.

The micro-mechanical parameters used for this work are presented in Table 1. Note that they were not calibrated to any gouge material as the scope of the paper is not a one-to-one comparison with experiments, but rather a qualitative analysis. They are chosen, however, to be such that their values have a physical meaning and, at the same time, the maximum apparent friction of the gouge material to comply with the maximum friction of the Byerlee's law (Byerlee, 1978) that is, $\mu_{peak} = 0.85$ (we term friction coefficient the stress-ratio τ/σ_c hereafter, see also Appendix B). The values of particles' friction, ϕ, stiffness modulus, E and density, ρ are selected to be 30°, 63 (GPa) and 2,900 (kg/m^3) respectively, similar to the values used by Dorostkar et al. (2017a) for comparison to experiments. Finally, the values for rolling (and twisting) resistance are selected such that the particles would

Table 1
Micro-Mechanical Parameters of Gouge Material

Particles property (unit)	Value
E (GPa)	63
ϕ (°)	30
ρ (kg/m^3)	2,900
α_s (-)	0.25
α_r (-)	0.1
η_r (-)	0.1
α_{tw} (-)	0.1
η_{tw} (-)	0.1

correspond to angular shaped grains, more specifically between rectangular and pentagonal (in 2D) according to Estrada et al. (2011).

2.4. Scaling

For accelerating the simulations, a scaling procedure will be used, which will allow us to work on a mechanically equivalent system that requires minimum calculation time. In order for this system to be adequately scaled, the related time-scales and length scales of the original and the scaled systems have to be appropriately selected, as explained below, to ensure that for the selected parameters the system is described by the same type of shear-physics as the original system.

We will start the scaling by identifying characteristic times and lengths involved in the specific system. The granular system is mainly described by its inertia and stiffness. In the following, the inertia and stiffness limits of the whole system are explained, leading to the dimensionless quantities that describe it.

However, the parameter selection should also favor the stability of the algorithm. The stability of the numerical scheme is thus derived for the general case and the related critical time-steps are defined. The final parameters selection will be based on both the granular physics description and the numerical stability of the algorithm.

2.4.1. Quasi-Staticity of the Problem

The behavior of granular materials can be classified in three main different regimes: quasi-static (solid-like), dense flows (fluid-like), and collisional (gas-like; Aharonov & Sparks, 2002; MiDi, 2004; Radjaï & Dubois, 2011). These regimes are defined by two dimensionless numbers. The first one, the *inertial number*, I, is the ratio of timescales imposed by the stress, shear rate, and momentum and is given by (Koval et al., 2009; MiDi, 2004; Radjaï & Dubois, 2011; Rognon et al., 2006, 2008):

$$I = \dot{\gamma} d_{50} \sqrt{\frac{\rho}{\sigma_c}} \tag{3}$$

where $\dot{\gamma}$ is the shearing rate.

According to MiDi (2004), Radjaï and Dubois (2011), and Rognon et al. (2008) on high inertial numbers, $I > 10^{-1}$, the behavior of the material is similar to that of a non-well structured network with spontaneous collisions between particles and very short force-chains between particles that disappear almost instantly. For intermediate inertia numbers, $10^{-3} < I < 10^{-1}$, the material behaves as a homogeneous shear flow, whose viscosity is controlled by the inertia number and can be translated as a state in the constitutive law for the material. The network is dense and the force chains are longer than the collisional regime. Finally, for low inertial numbers, when theoretically $I \to 0$ or, practically, $I \ll 10^{-3}$, the material behaves quasi-statically. In the later case, any related rate-effects on the global behavior of the granular material are negligible and the grains network is dense, well-coordinated with the force-chains well defined across many particles. Moreover, the material behaves as a solid (which might show dependency on the dimensional stiffness of the granular packing, κ, see next paragraph) and eventually reaches a state in which it can undergo infinite plastic isochoric deformation under constant load, which corresponds to the well-known "critical-state" as defined in soil mechanics (Wood, 1990). The critical state of a granular material strongly depends on its friction coefficient, rolling resistance (Radjaï & Dubois, 2011) and fabric (Li & Dafalias, 2012). Note that this classification scheme is based on monodisperse distributions. However, at the range of polydispersity studied in this work, this classification still holds (Shire et al., 2021). The evolution of I with depth is presented in Figure 2 for a constant density of $\rho = 2{,}900$ (kg/m^3). In the same figure, the shearing regime of a gouge layer with a thickness of $H \simeq 70$ particles, as considered in this study, is compared to different cases of normalized layer thicknesses and shearing velocities. The represented conditions correspond to a high seismic shear velocity of $v_s = 2.0$ (m/s) and in situ effective stress based on $\sigma_c = \rho g z - \rho_w g z$, with ρ_w the density of water. It is shown that lower velocities and larger layer thicknesses favor quasistatic response of the medium.

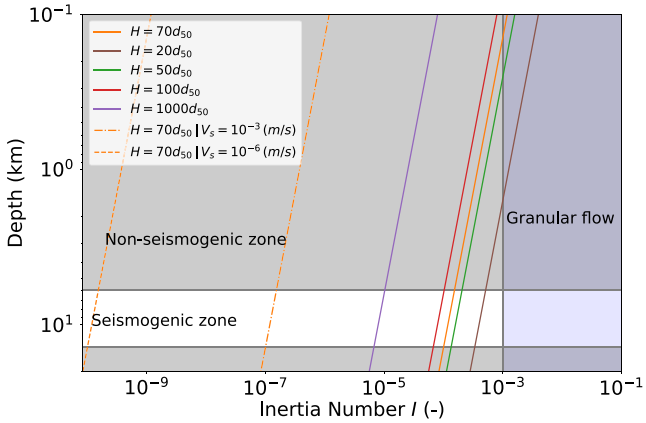

Figure 2. Inertia number evolution with depth for different shearing velocities V_s and normalized layer thickness, H/d_{50}. The blue shaded area corresponds to granular layer in dense shear flow regime and the dark shaded area to non-seismogenic zones.

Given the physical restrictions on pre- and co-seismic velocity, which is several orders of magnitude lower than 2.0 (m/s) and on the ratio of gouge layer over particle size, which is similar or higher than $H \simeq 70d_{50}$ for real fault cores (Chester & Chester, 1998), this trend can be considered as an upper limit inertia number evolution versus depth for the conditions studied hereafter.

The second dimensional number characterizing granular material flow regime is the dimensionless stiffness number, $\kappa = \frac{k_n}{\sigma_c d_{50}}$ (for linear contacts in 3D). κ describes the effect of contact strains of order $\mathcal{O}\left(\kappa^{-1}\right)$ to strains from network re-organization on the global behavior of the packing. For $\kappa \gg 1$, the rigid grain limit is met and the DEM granular material's mechanical response becomes independent of κ (Hosn et al., 2017; Radjaï & Dubois, 2011). As a result, any scaling of stiffness that returns a κ above the rigid grain limit, should not affect the mechanical response of the system.

2.4.2. Critical Timesteps

The generalized dynamics for the granular assembly are given by:

$$\mathbf{M}\ddot{\mathbf{x}}(t) + \mathbf{C}\dot{\mathbf{x}}(t) + \mathbf{K}\mathbf{x}(t) = \mathbf{F}(t) \tag{4}$$

$$\mathbf{J}\ddot{\boldsymbol{\theta}}(t) + \mathbf{C}\dot{\boldsymbol{\theta}}(t) + \mathbf{K}_{r,tw}\boldsymbol{\theta}(t) = \mathbf{T}(t) \tag{5}$$

where, $\boldsymbol{x}$ is the displacement of particles at time t and their first and second time derivatives $\dot{\boldsymbol{x}}, \ddot{\boldsymbol{x}}$ are their translational velocity and acceleration, respectively, at time t (s). The matrices $\mathbf{M}$, $\mathbf{C}$, and $\mathbf{K}$ are the global mass matrix, a drag force matrix by the viscosity/damping exerted on particles and the generalized stiffness matrix describing the stiffness of contacts of each particle. Finally, $\boldsymbol{F}$ is the resultant force exerted on the particles at time t. Similarly, θ is the rotation vector of the particles at time t and, $\dot{\boldsymbol{\theta}}$, and $\ddot{\boldsymbol{\theta}}$ the rotational velocity and acceleration, respectively. The matrices $\mathbf{J}$, $\mathbf{C}$, and $\mathbf{K}_{r,tw}$ are the moment of inertia, any viscous dissipation on rotation and the rotational/twisting stiffness. $\mathbf{T}$ is the resultant external torque applied to the particles.

The discretization of the above set of equation in the finite difference scheme requires a maximum time-step for numerical stability of the algorithm. This critical timestep, in absence of damping is (Šmilauer et al., 2021):

$$\Delta t_c^k = \sqrt{\frac{2m}{k_n}} \tag{6}$$

$$\Delta t_c^r = \sqrt{\frac{2\mathrm{j}}{k_r}} \tag{7}$$

where Δt_c^k and Δt_c^r are the critical timestep emerging from translational and rotational degrees of freedom, respectively. m, $k_n = ER$, j and k_r are the particles' mass, stiffness, moment of inertia, and rotational stiffness, respectively, which are selected in such a way to minimize the critical timesteps. The resulting critical timesteps are in agreement with the findings of Hosn et al. (2017).

Furthermore, in the extreme case when there is no active contact on a particle, the above timesteps are impossible to be calculated ($k_n = 0$). In this case, the timestep is calculated based on the sonic wave velocity (Šmilauer et al., 2015) and it is equal to:

$$\Delta t_c^p = R\sqrt{\frac{\rho}{E}} \tag{8}$$

The critical timestep that will be governing the numerical problem should be $\min\left\{\Delta t_c^k, \Delta t_c^r, \Delta t_c^p\right\}$.

2.5. Equivalent System

In this section, it is explained how a new system, which is equivalent to the original one in terms of shear mode (defined by its inertia and stiffness), can be simulated through scaling in order to achieve a computationally affordable model. In the following, a scaling analysis is presented in which, starting from the reference

Table 2
Mechanical Properties of the Reference Fault System

Property (unit)	Value
E^* (GPa)	63
ρ^* (kg.m^{-3})	2,900
d_{50}^* (μm)	90
v_s^* (m.s^{-1})	2.0
σ_c^* (MPa)	160

system, corresponding here to the gouge material under seismic slip in the seismogenic zone's conditions, we find an equivalent system, which keeps the mechanical behavior of the reference system unaffected, but reduces the computational cost to minimum. To do so, a density scaling procedure is taken into account.

The values on Table 2 describe the reference system. From these values, using the definition of the inertia number in Equation 3, the system's response to shear loading falls in the quasi-static regime $I^* = 1.3 \times 10^{-4} < I_{\max} = 10^{-3}$. Consequently, according to Section 2.4.1, the system responds quasi-statically.

Due to computational restrictions related to the critical time-step of the numerical integration scheme, which, at the studied conditions could reach below 10^{-9} (s) (according to Table 2), simulating the exact conditions of the fault gouge in the seismogenic zone can be prohibiting. Combining equations Equation 3 for the inertia number, I, and Equations 6–8 for the critical timesteps of the system, the critical timesteps are expressed as a function of the inertia number as follows:

$$\Delta t_c^k = \sqrt{\frac{2m}{K}} = \left(\frac{1}{\dot{\gamma}}\sqrt{\frac{2\sigma_c}{3E}}\right) I \tag{9}$$

$$\Delta t_c^p = \frac{d_{50}}{2}\sqrt{\frac{\rho}{E}} = \left(\frac{1}{2\dot{\gamma}}\sqrt{\frac{\sigma_c}{E}}\right) I \tag{10}$$

In order to obtain the maximum timestep for which the system will remain in the quasi-static regime ($I \leq I_{\max}$), we solve the relation for the critical timestep, using the maximum allowed inertial number $I_{\max} = 10^{-3}$. We obtain: $\Delta t_c^k = 0.5 \times 10^{-7}\,(s)$ for the DEM system, while the critical time-step for the real system corresponds to $\Delta t_c^{k*} = 6.4 \times 10^{-9}\,(s)$. Using this scaling in time, our simulations can be accelerated by one order of magnitude. This is of particular importance given the stochastic approach followed herein and presented in Section 3.

Naming the ratio between the DEM time-step and the real one ζ, the scaled density of the particles of the DEM system in order to be equivalent to the real one is (assuming $E = E^*$ and $d_{50} = d_{50}^*$):

$$\zeta = \frac{\Delta t_c^k}{\Delta t_c^{k*}} = \frac{d_{50}\sqrt{\frac{\rho}{E}}}{d_{50}^*\sqrt{\frac{\rho^*}{E^*}}} = \sqrt{\frac{\rho}{\rho^*}} \Rightarrow \rho = \zeta^2 \rho^* \tag{11}$$

In this case $\zeta \simeq 8$, thus $\rho = 64\rho^* = 64 \times 2{,}900$ (kg.m^{-3}). In other words, we increase the density of the particles to speed-up the calculation time and keep the mechanical behavior of the system unaffected. Notice that this is the maximum speed-up allowed in this case, as higher ρ would violate the quasi-static regime of granular flow and would alter the physics of the problem.

3. Stochastic Interpretation

Earthquakes depend on the frictional properties of the fault system. The term frictional properties, refers to the apparent mechanical behavior of a Representative Elementary Volume (REV) of the granular gouge material, which emerges from the collective behavior of individual grains inside the REV during shearing. Over the whole surface of the fault, which has an area $\sim L \times L$ and thickness H, the properties of the gouge and packing of the granular material are heterogeneous and random. This randomness is considered in our analysis using the Monte-Carlo method. More specifically, in order to account for this randomness, we consider multiple tests on a smaller, periodic SEV, of characteristic size l, which after averaging will lead to the REV, of characteristic size, L^{REV}, that is seen here as an intermediate scale (meso-scale), see Figure 1. According to Ostoja-Starzewski (2006), the SEV has to contain enough particles in order to be representative and, consequently, its characteristic size, l, has to be larger than the characteristic size of the grains, that is, $l > d_{50}$. Here, $l \simeq 20\, d_{50}$ in length, $6\, d_{50}$ in width and $H \simeq 70 d_{50}$ in height. Adopting scale separation $L \gg L^{REV} > l$, $w > d_{50}$ (Ostoja-Starzewski, 2006).

In systems with few particles, the overall frictional response of the granular layer is expected to arise from repetitive cycles of stick and slip behavior. These cycles will emerge from the periodic grain force chains buildup-collapse.

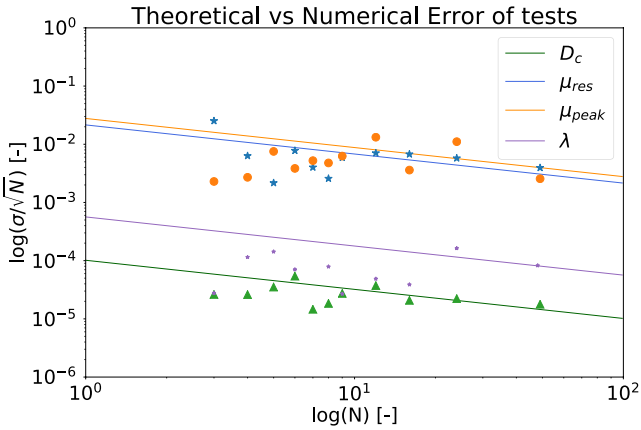

Figure 3. Monte-Carlo error-convergence for 50 tests with $d_{50} = 90$ (μm), $f = 0.0$ and $V_s = 2$ (m.s^{-1}).

We will refer to this effect as *local* stick-slip motion hereafter. In systems with higher geometrical complexity, for example, more particles across the height, width, and length of the gouge layer, the local stick-slip may play a less prominent role due to the large extent of states of internal re-organization of the granular layer. Taking into account the size of the fault zone interface compared to the size of the fault gouge particles, many geometrical variations can emerge in the spatial arrangement of gouge particles. Furthermore, if the conditions allow for strain localization to take place, a thin zone in which most of the deformation takes place may appear, which represents a self organization of the system toward a critical state (Bak et al., 1988).

Moreover, in order for the local stick and slip motion to be persistent at the large scale, the particles should be equally distributed in space over the complete length and width of the fault. If this is not the case, the local slip at some small part of the fault can be counter-balanced by a synchronous stick at a small part near by it.

For the above reasons, we will present here an analysis based on the stochastic interpretation of several tests of SEVs, which, after averaging, represent the frictional behavior at the scale of the REV. The minimum number of SEV tests, N, that, after averaging, provide an adequate, representative description of the frictional response at the level of the REV is determined using the Monte-Carlo error estimation (see Appendix C for details about bounding the error in the prediction of the mean quantities of interest).

The error convergence for the different quantities of interest (critical slip distance D_c, the residual friction angle, μ_{res}, the peak friction angle, μ_{peak}, and shear band thickness λ) is shown in Figure 3. The values are oscillating around the theoretical error prediction and then fairly converge toward it. It is thus justified that, in our case, a total of 50 averaged tests is adequate to describe the response and the related apparent frictional behavior of the fault gouge.

The response of the representative sample will now be as appears in Figure 4 (right). In this figure, the friction drop related to the global slip-weakening behavior of the material is denoted as $\Delta\mu^g$, while friction drops related to local stick-and-slip dynamics are denoted by $\Delta\mu^l$. Comparing it to the behavior of a single test Figure 4 (left), it becomes evident that the local stick-slip events tend to vanish with increasing number of tests and thus its role is negligible for the overall, apparent frictional behavior of the granulated fault gouge. This stochastic approach renders this work fundamentally different from previous analysis with DEM, where the authors are focusing on single analysis and they did not take into account the stochastic nature of the problem at hand.

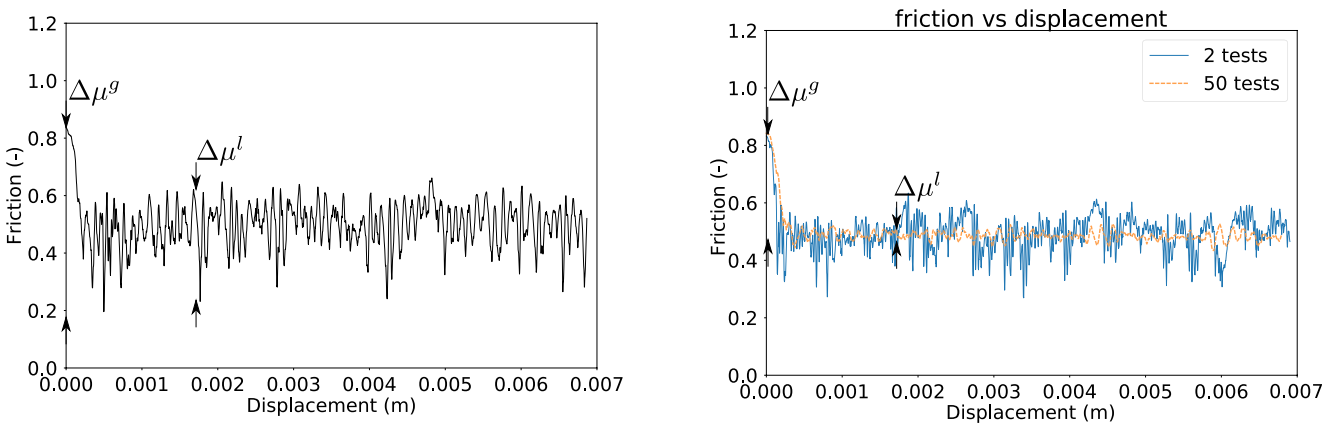

Figure 4. (left) The plastic (post-peak) branch of the frictional response of a single test and (right) the averaged responses of 2 and 50 tests on specimens with $d_{50} = 90$ μm and $f = 0$. The effect of averaging on local and overall, apparent quantities (superscript ^{l} and ^{g} respectively) is demonstrated.

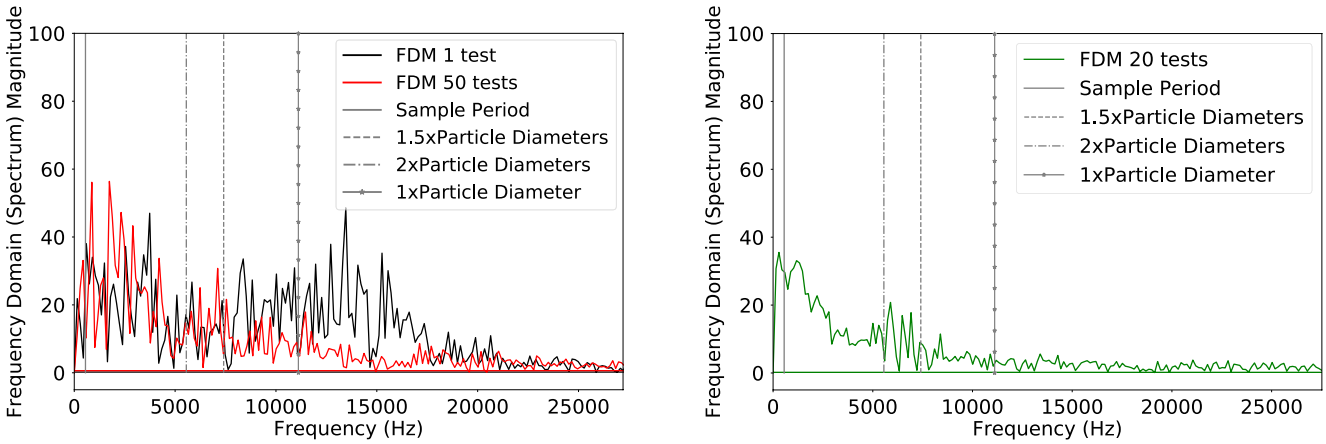

Figure 5. (left) The average (power) spectra of individual tests shows a clear peak at the frequency related to $1.5d_{50}$. Displacements for related to $1.5d_{50}$ scales are thus expected to be important for single tests. (right) Response spectrum of the averaged tests shows minimal impact of high frequencies. Thus, the behavior seems not to depend on grain-scale related displacements. In all cases, the sampling frequency was $f_s = 1.11$ MHz.

3.1. Spectrum and Filtering

Using discrete Fourier transform the following properties emerge for the system. Single tests show, a large density of events correlated to frequencies related to $1.5d_{50}$. These events correspond to local stick and slips. However, these events are completely missing from the averaged response. In Figure 5, we present the mean of the response spectra of single tests together with the response spectrum of the averaged. This corroborates the negligible role of the local stick-slips in the global apparent friction of the granulated fault gouge.

What is even more interesting is that, the total dissipated energy (calculated as $E_{dis} = \int F_s \delta_s d\delta_s + \int F_n \delta_n d\delta_n$, δ_n being the dilation and δ_s the slip) in the averaged ensemble and single tests, is practically the same (with a relative average absolute error of 4%), for the ensemble and single tests. This can also be explained figuratively. One can think of the ensemble as in Figure 1 with the SEVs placed along the width. A local slip event might take place in one SEV (dissipating energy) while simultaneously a stick phase might be taking place in another SEV (building up energy).

The aforementioned statistical analysis enables us to determine the global apparent frictional properties of the gouge with less analyses. Specifically, since the hi-frequency signal is irrelevant for the apparent global frictional response, a Butterworth low-pass filter is applied on the responses to remove the high-frequency noise related to phenomena of the level of the grain size. In Figure 6, it is shown that if a cutoff frequency of 1/1.5 d_{50} is used on 20 averaged tests, it confirms the resulting response is almost identical to the 50 tests case. Thus, for all tested scenarios in the following sections, and in order to reduce the calculation cost, 20 tests are ran, averaged and filtered as above to obtain the global response.

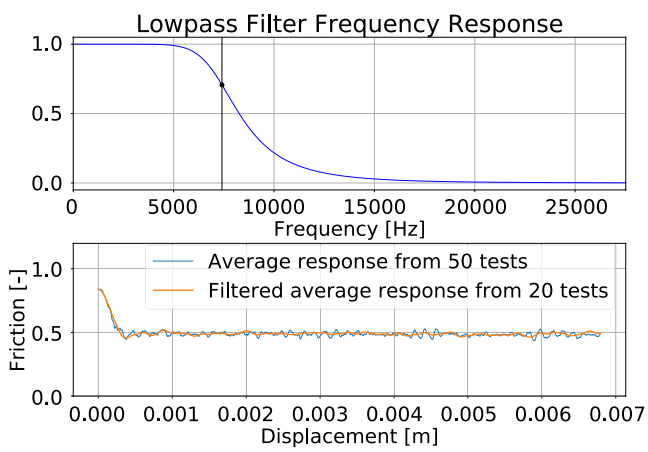

Figure 6. Butterworth low pass filter applied on data obtained by 20 tests to remove the high-frequency noise. The cutoff frequency of the filter is set at 1/2 d_{50}. The response of 20 tests, filtered, is approaching the one of 50 tests.

4. Results

Based on the assumptions justified above, a series of tests were done to study the influence of particle characteristics, such as the mean particle diameter, d_{50}, and the PSD width, f, on the apparent frictional behavior of the gouge analog and the slip-weakening behavior that will finally control the fault's stability. Furthermore, the frictional response of different shear-rates was studied in order to study the existence of velocity-weakening apparent frictional behavior of the gouge, as it controls the stability of the granular interface (see Section 2.2). The tests description is summarized in Table 3. All tests were performed under constant normal stress, $\sigma_c = 160$ (MPa).

Table 3
Tests Performed

Name	Description	Number of tests
90*f*#0.0	$d_{50} = 90$ (μm), $f = 0.0$, $H = 6$ (mm)	20
90*f*#0.5	$d_{50} = 90$ (μm), $f = 0.5$, $H = 6$ (mm)	20
90*f*#0.7	$d_{50} = 90$ (μm), $f = 0.7$, $H = 6$ (mm)	20
60*f*#0	$d_{50} = 60$ (μm), $f = 0.0$, $H = 5$ (mm)	20
120*f*#0	$d_{50} = 120$ (μm), $f = 0.0$, $H = 8$ (mm)	20
V_s#1	90*f*#0, $V_s \times 10^{-3}$	20

4.1. Apparent Frictional Response - Macroscopic Slip Weakening - Critical Slip Distance D_c

The emerging peak and residual friction coefficient of the granular layer during shearing will define the friction drop $\Delta\mu$. According to Section 2.2, any parameter that affects the friction drop could be directly related to the stability of the system. It is worth mentioning that the "peak" (also called "maximum") and the "residual" friction are often referred to in the literature as "static" and "kinetic" friction, respectively. The terms "dynamic" or "steady-state" are used to describe the kinetic friction. The peak friction is associated with higher frictional strength at the onset of sliding (stick/static phase). This friction must be exceeded for slip to commence, during which slip is resisted by a dynamic friction, which is usually lower (see also Byerlee, 1978; Dieterich, 1979; Kanamori & Brodsky, 2004; Rabinowicz, 1951, 1958; Scholz, 2002). The transition from the static to the dynamic friction is performed in a characteristic slip distance D_c as we also observed in our simulations.

The apparent frictional response of the averaged tests is compared here for tests on samples containing different PSD widths f and different mean particle sizes d_{50}. The frictional response of the related tests is presented in Figure 7. The shear-tests for distributions defined by $f = 0.0$, $f = 0.5$, and $f = 0.7$ (tests 90*f*#0.0, 90*f*#0.5, 90*f*#0.7 of Table 3) are shown for mean particle diameter $d_{50} = 90$ (μm). The peak and residual friction coefficients and the resulting friction-drop magnitude for all cases is summarized in Figures 8a, 8c, and 8e. The results demonstrate that there is minimum effect of distribution width on the apparent friction of the granular layer. Several authors considered the width of the PSD as a stabilizing parameter (see Anthony & Marone, 2005; Mair et al., 2002; Morgan & Boettcher, 1999, among others). Although they are right about the fact that the parameter f controls the local stick-slip magnitude, in the stochastic case studied here it is found to control how fast the local stick and slips (or, the high-frequency noise) are vanishing with increasing width of the fault gouge. Thus, the PSD width property is not directly related to the apparent frictional stability of the fault system, according to the analysis performed here.

Similarly, the effect of particle size of the gouge granular analog on the apparent friction is presented on the same plots in Figures 7, 8b, 8d, and 8f for tests on mean particle diameters of $d_{50} = 60$, 90, and 120 (μm) (tests 90#*f*0.0, 60*f*#0.0, 120*f*#0.0 in Table 3). As for the case of PSD width, the mean particle size is found to play no important role on the emerging macroscopic friction coefficient evolution. This is not a surprising result (see Cantor et al., 2018; Voivret et al., 2009). However, our simulations show evidence that the PSD does not have a significant impact on the peak friction coefficient as well. Nevertheless, according to Figures 8e and 8f, the slip distance, D_c, for the transition from the peak to the residual apparent friction coefficient, scales with the mean particle size.

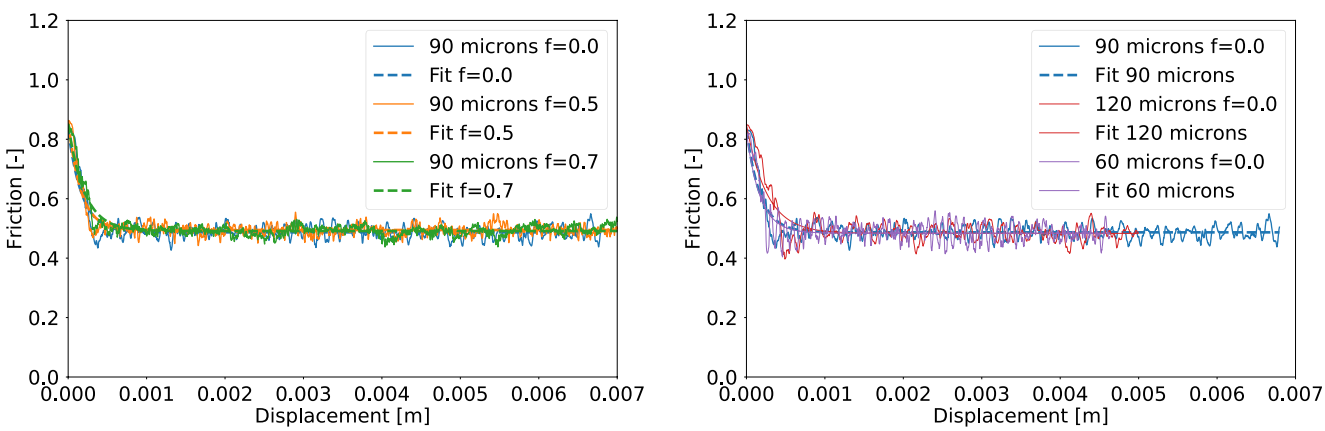

Figure 7. Frictional response of averaged tests for different particle size distributions ($f = 0$, 0.5, 0.7), left, and particle size ($d_{50} = 60$, 90, 120 (μm)), right.

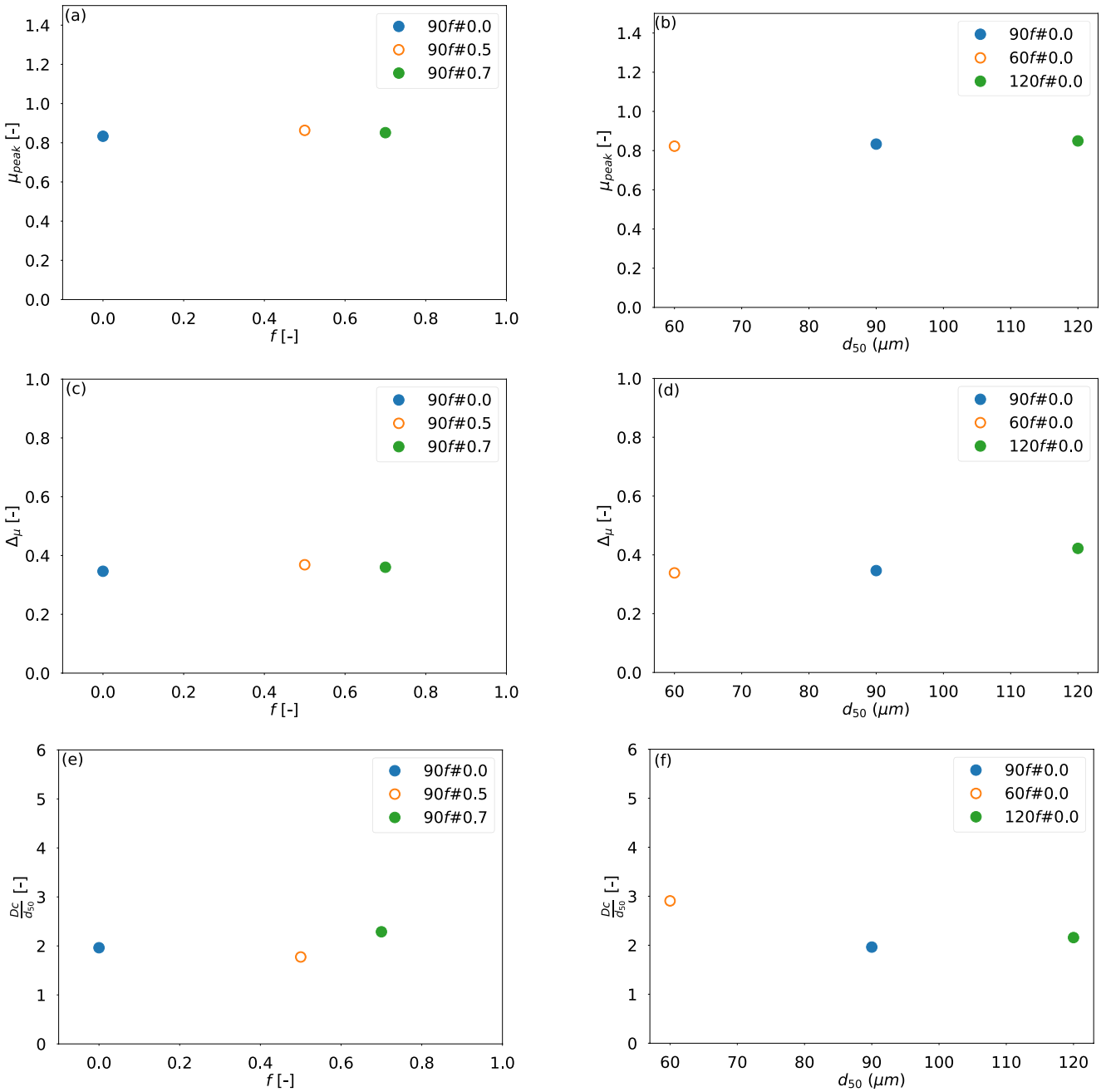

Figure 8. (top plate: a, b) Emerging peak and residual friction angle, (middle plate: c, d) friction drop, (lower plate: e, f) critical slip distance, D_c, for different particle size distributions, f, and mean particle diameters, d_{50}, respectively.

One of the main characteristics that describes the apparent frictional behavior of a fault is the above mentioned critical slip distance D_c (Dieterich & Carter, 1981; Scholz, 2002). D_c is the displacement that has to be carried over for the transition from peak (static) friction to residual (dynamic) friction. D_c plays a very important role on the dynamic stability of the system at a given depth, along with the friction drop described previously, as they both determine the amount of mechanical softening with slip.

In the following, the critical slip distance, D_c, is estimated from the interpolation of the averaged friction response at softening with the exponential decay function (Platt et al., 2014; Rattez, Stefanou, Sulem, Veveakis, et al., 2018):

$$\mu = \mu_{res}\left(1 + \frac{\Delta\mu}{\mu_{res}} e^{-\delta/D_c}\right) \tag{12}$$

where μ_{res} is the residual friction coefficient, $\Delta\mu = \mu_{peak} - \mu_{res}$ the variation between the maximum and residual friction coefficient, D_c the characteristic slip distance and δ the total slip distance.

The interpolation with the exponential decay law of Equation 12, is plotted against the related averaged frictional response in Figure 7. It is shown that the mean critical slip distance in tests of different PSDs, varies for the different distributions, but does not scale with the width of the PSD, f. Consequently, the width of the distribution does not seem to play a stabilization role on dry gouge shearing, as previously postulated by other studies focusing on local stick-slip events (e.g., Anthony & Marone, 2005; Mair et al., 2002; Morgan & Boettcher, 1999).

Regarding the effect of mean particle size, d_{50}, on the critical slip distance, Figures 7 and 8 (lower plate) show that D_c does scale with the particle size d_{50}. Consequently, the apparent slip-weakening behavior of the fault gouge can be described as a function of the mean grain size. The relation of critical slip distance, D_c with d_{50} (or another measure of the PSD) is important aspect in modeling as it gives a justifiable and measurable characteristic length, that of the mean particle diameter, d_{50}, to the problem for detailed macroscopic modeling (e.g., Collins-Craft et al., 2020; Rattez, Stefanou, Sulem, Veveakis, et al., 2018).

4.2. Shear Band Thickness

The shear band thickness was measured by interpolating the total shear strain accumulated in the sample. The interpolation function used is a trigonometric function previously used by Rattez, Stefanou, and Sulem (2018), and Rattez, Stefanou, Sulem, Veveakis, et al. (2018).

The width of the localized deformation zone will govern the response of the softening branch of frictional response. Thus, one of the most important pieces of information we can get from the present DEM analyses is the physically emerging width of the shear band of the gouge material and its evolution during shearing. Passing from displacements to deformation for the sheared layer requires an equivalent continuum representation. Here, the specimen is first discretized in equal-width horizontal zones of height Δh. Then, the average strain $\langle \gamma_s^i \rangle$ and average strain rate $\langle \dot{\gamma}_s^i \rangle$ are calculated for each zone, i, as follows:

$$\langle \dot{\gamma}_s^i \rangle \triangleq \frac{\langle v_x^i \rangle - \langle v_x^{i-1} \rangle}{\Delta h}, \langle \gamma_s^i \rangle \triangleq \int_0^t \langle \dot{\gamma}_s^i \rangle dt \tag{13}$$

where $\langle v_x^i \rangle$ is the average velocity component in the direction of shear for the zone i.

The shear band thickness (which can be related to the width of the principal slip zone, or PSZ, a zone of intense deformation which is often observed in fault cores outcrops) is then calculated based on the cumulative strain $\langle \gamma_x^i \rangle$, using the following trigonometric interpolation function:

$$\Gamma_s(z) \approx B\chi_{\left[Z-\frac{\lambda}{2};Z+\frac{\lambda}{2}\right]}(z)\left[\cos\left(2\pi\frac{(z-Z)}{\lambda}\right) + 1\right] \tag{14}$$

with B being twice the maximum strain, Z being the coordinate of the center of the shear band, λ the wavelength of the cosine function and $\chi_{\left[Z-\frac{\lambda}{2};Z+\frac{\lambda}{2}\right]}$ the rectangular function defined by:

$$\chi_{\left[Z-\frac{\lambda}{2};Z+\frac{\lambda}{2}\right]}(z) = \begin{cases} 1 & \text{if} z \in \left[Z-\frac{\lambda}{2}; Z+\frac{\lambda}{2}\right] \\ 0 & \text{otherwise} \end{cases} \tag{15}$$

Z and λ are unknowns to be determined from the velocity profiles by the DEM analysis. The wavelength of the cosine function is interpreted as the shear band width.

Applying the above interpolation at the final stage of shear loading allows for estimation of the shear band thickness. In the top plate of Figure 9, the shear band thickness of tests corresponding to different PSDs and shearing velocities are shown along with its variance (denoted with error-bars). The lower plate of Figure 9 shows the

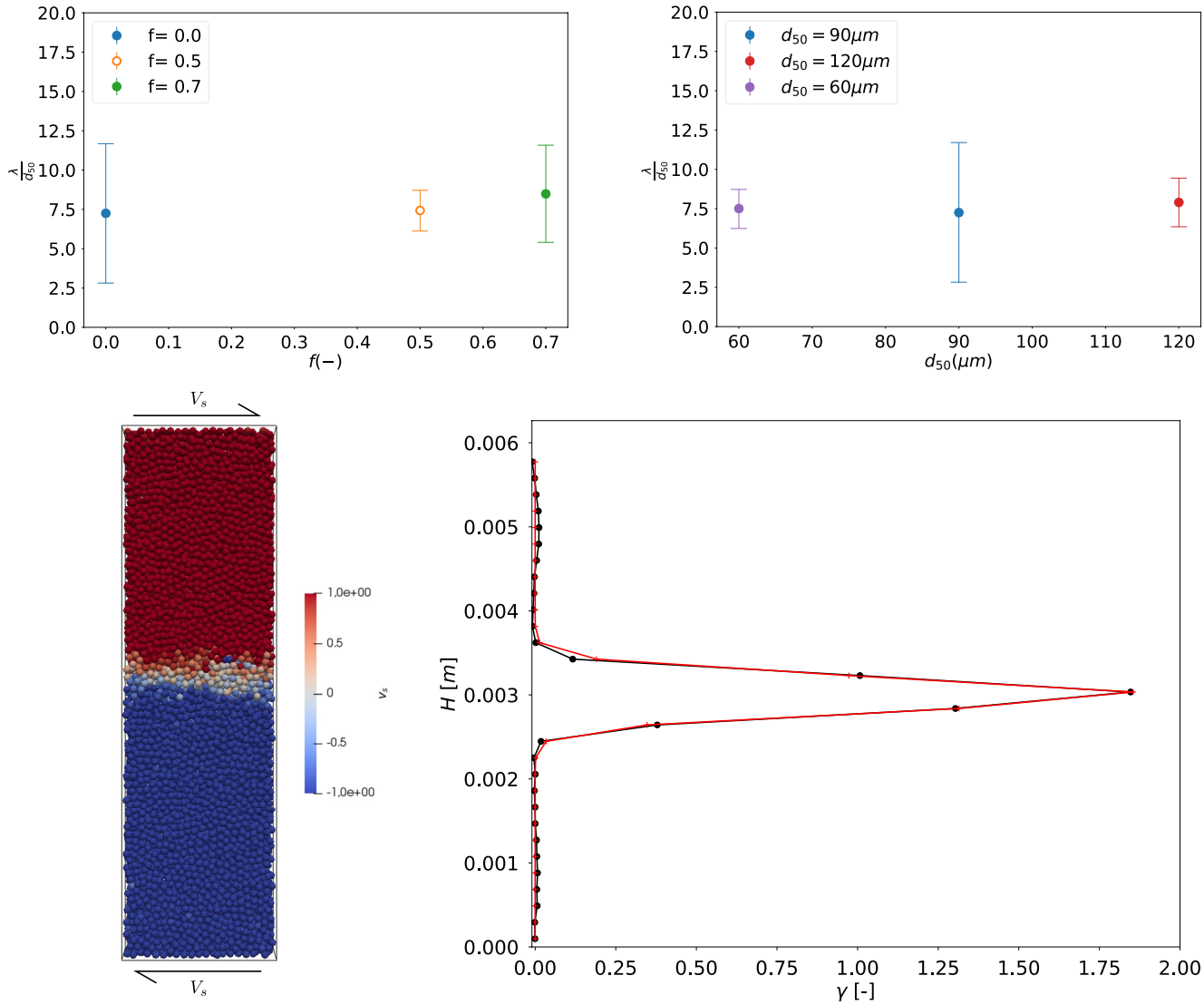

Figure 9. (top plate) Mean value and variance of the final band width compared between different particle size distributions of width f and for mean particle diameters, d_{50}. (lower plate) Velocity profile across the height of the specimen and the resulting localization of deformation.

non-smooth velocity gradient across the specimen. The shear band is usually forming close to the center of the specimen. In some cases, however, it might form closer to the boundaries. In these cases, the shear band thickness is not taken into account in the statistical analysis, to exclude any parasitic effects related to the boundary conditions. The shear band width was measured at the steady state, after a total slip of ~ 6–10 (mm) or $4 \times l$ after, that is, shearing displacement significantly larger than characteristic slip distance, D_c. The shear band width, normalized by the mean particle size, d_{50}, remains almost constant among tests. This justifies why D_c scales with d_{50}. It also justifies recent studies with continuum approaches that take into account the size of the microstructure (e.g., Mühlhaus & Vardoulakis, 1987; Rattez, Stefanou, Sulem, Veveakis, et al., 2018). These studies show also the connection of the shear band thickness with the size of microstructure.

4.3. Rate Dependency

Finally in terms of shearing velocity, no influence of the slip-rate on D_c was observed for tests with the same inertia number conditions. Shearing velocity tests for $V_s = 2$ (m/s) and 2×10^{-3} (m/s), on the same packings, exhibit no difference on the global behavior caused by shear velocity (see averaged and interpolated results in Figure 10). Peak friction and residual friction values, μ_{peak}, μ_{res}, are almost identical for all the tests and the same

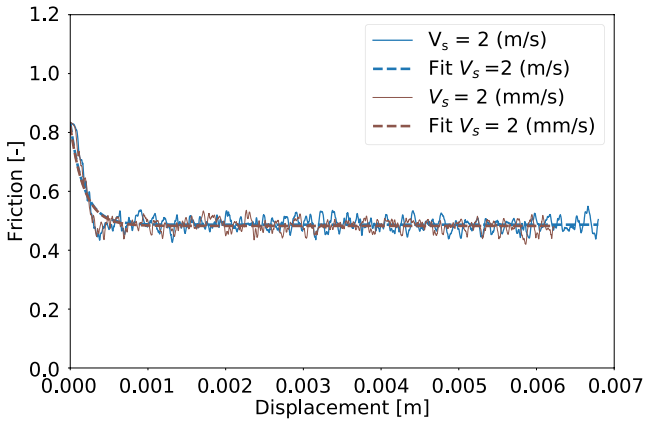

Figure 10. Frictional response of averaged tests for shearing velocities $V_s = 2$ (m/s) and $V_s = 2$ (mm/s).

applies to the critical slip distance, D_c, independently of the applied slip-rate (see Figure 11 lower plate).

The results are in accordance with previous findings in the mechanics of granular materials, which suggest that if the sample remains in the quasi-static regime the global response is unaffected by the loading rate (here the slip-rate) and the fluctuations in apparent friction are of higher orders, caused by local inter-granular inertial creep (Radjaï & Dubois, 2011). As mentioned in Section 2.4.1 for a fault gouge at several kilometers depth, the inertial number is of the order of $I \simeq 10^{-4}$ or less during co-seismic slip, which always falls into the quasi-static regime. Consequently, there is no slip-rate weakening observed for the dry granular system under the studied conditions.

In order to investigate the appearance of rate-and-state dependency on the response, a velocity-stepping simulation is carried out following similar protocols with Dieterich and Carter (1981), Ruina (1983), and Verberne et al. (2020). Experimental results have shown the existence of such viscous effects during shear-rate changes (Beeler et al., 1994; Biegel et al., 1989; Chambon et al., 2002; Dieterich, 1979). In the following test, the initial shearing velocity is set to $V_s^0 = 2$ (mm/s) and after ~7 (mm) of shear displacement, that is, in the so-called steady-state regime, the shearing velocity is lowered to $V_s = 0.2$ (mm/s). This protocol allows the identification of "velocity-weakening" effects, in the frame of the rate-and-state friction law terminology. More specifically, in this framework, "velocity weakening" refers to the difference of the steady

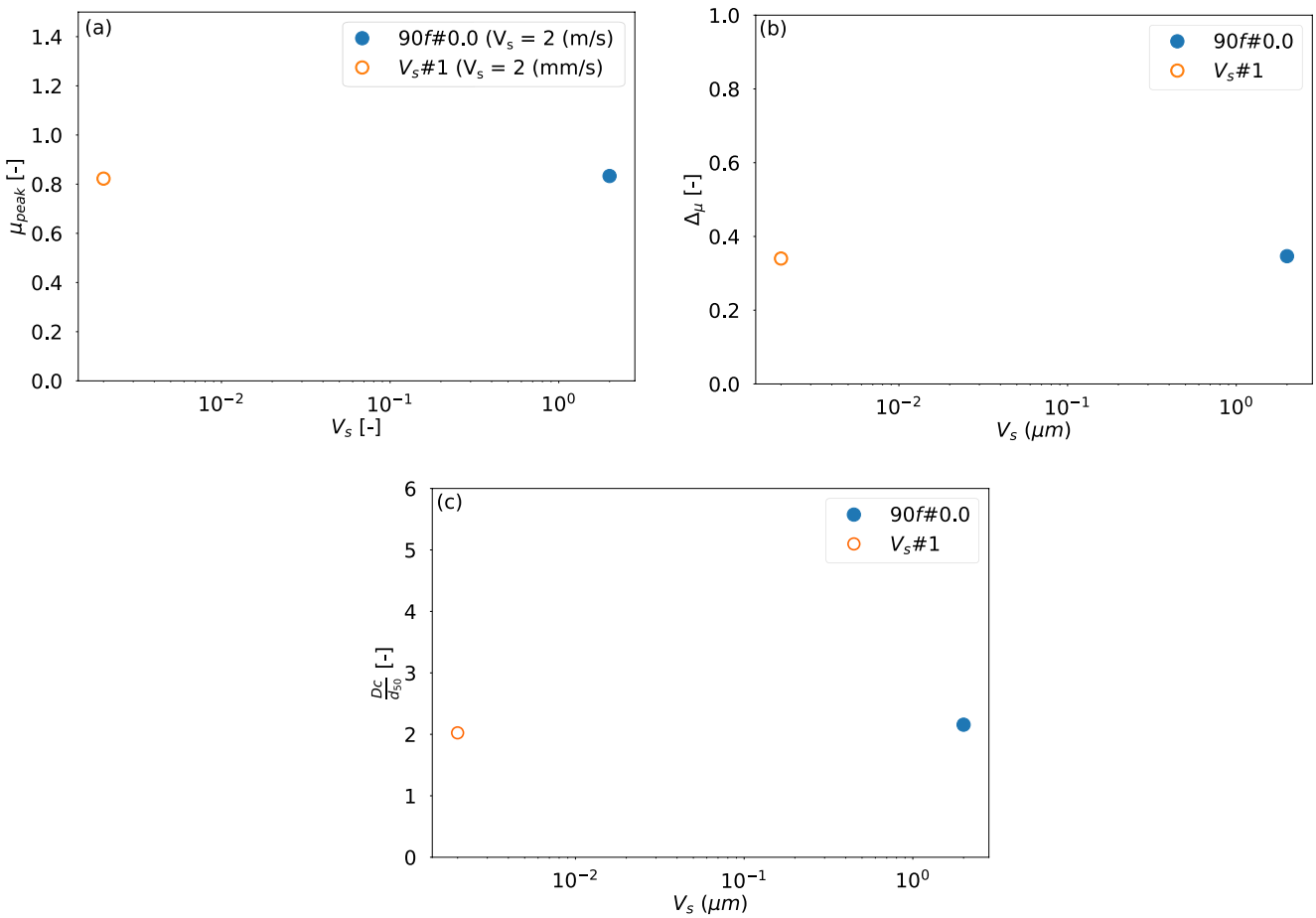

Figure 11. (top left) Emerging static and dynamic friction angle, (top right) friction drop, (lower plate) critical slip distance D_c, for different shearing velocities V_s.

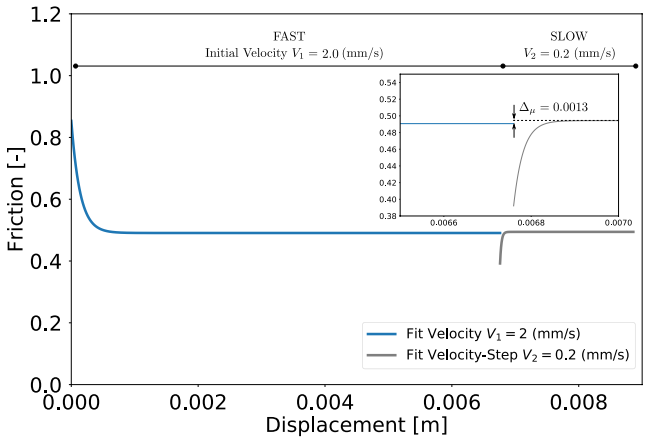

Figure 12. Comparison of residual friction coefficient during velocity-stepping test. The specimen is sheared at a velocity $V_s = 2.0$ (mm/s) initially, then suddenly to a slower velocity $V_s = 0.2$ (mm/s).

state friction coefficient before and after a shear velocity change is applied (Dieterich & Kilgore, 1994; Marone, 1998; J. R. Rice, 1993; Ruina, 1983).

In Figure 12, the steady state friction is compared between the case V_s#1 sheared at 2.0 (mm/s) and after a change in shear velocity, V_s at the end of the test, at a lower velocity, $V_2 = 0.2$ (mm/s). The obtained response shows a difference of $\Delta\mu_{ss} \approx 0.00013$. The difference in the steady state friction coefficient, is about two orders of magnitude lower than the measured friction drop promoted by the slip-weakening behavior at the onset of sliding. However, this drop of the steady state friction coefficient, is at the limits of the variance of the measured frictional response (for number of samples $N = 20$). Therefore, it should be considered with care due to the noise related to the repeated local stick-and-slip events that were observed in our simulations even after averaging over 20 samples (Monte Carlo simulations statistical ensemble, see Section 3).

5. Discussion

The material studied here mimics a material, which has undergone a severe cataclasis and large confinement for a long time. That is, after the long consolidation phase, the gouge particles are considered to be fragmented and angular with high resistance to rolling (this has been simulated numerically by spherical particles, but with relatively high rolling resistance values, see Estrada et al., 2011). This material is stiff, well coordinated, and highly interlocked before the slip takes place. As opposed to previous studies on glass-beads or DEM (Abe et al., 2002; Abe & Mair, 2009; Aharonov & Sparks, 1999, 2002; Anthony & Marone, 2005; Collettini et al., 2009; Guo & Morgan, 2006; Hazzard & Mair, 2003; Mair & Abe, 2008; Mair et al., 2002; Mair & Marone, 1999; Marone et al., 1990; Marone & Scholz, 1989; Morgan, 1999; Morgan & Boettcher, 1999), our granular material is under high confinement, and shows a high degree of interlocking. High interlocking and confinement, in this case result to a more intense friction drop in the material behavior as more effort is needed in order to overcome the maximum friction.

The conditions studied here are in analogy to the conditions taking place inside the seismogenic zone (Sibson, 2011). That is, large confinement, hard minerals, small mean particle size, and shear velocities spanning from slow to very rapid (for co-seismic slip). Under these conditions, it is shown that the fault gouge shears in the quasi-static regime, fails in brittle manner and eventually reaches a critical state regime. According to granular material mechanics, the behavior for quasi-static flows and granular materials in critical state does not depend on shearing velocity up to small order creep based fluctuations of $\Delta\mu \simeq 10^{-3}$ (e.g., Radjaï & Dubois, 2011). This is actually the case for the material's behavior. For shearing velocities between 10^{-3} and 1 (m/s) the global behavior is identical. The difference in steady state friction coefficient, although compatible with experimental findings (see Chambon et al., 2002), is about two orders of magnitude lower than the measured friction drop promoted by the slip-weakening behavior of the initial material. Contrary to the slip-weakening friction drop, such rate-effects are at the limits of variance of the frictional response. Indeed, several studies on rate effects needed an implementation of dynamic friction or rate-and-state friction laws at the contact scale (Morgan, 2004; C. Wang et al., 2019) in order to obtain an evident velocity weakening behavior. Even if the lower-order drops in friction are able to cause instabilities under such conditions, these small friction drops will be probably compensated by the geometrical disorder (variation) along the fault zone (Kanamori & Brodsky, 2004). What will control the system's stability finally is the massive drop in macroscopic, apparent friction.

One step further, probably due to the lack of an intense global friction drop in the non-interlocked assemblies, the aforementioned studies have been mostly focused on local stick and slip dynamics, that is, the periodical formation and breakage of grain force-chains. Although this mechanism takes place at the critical state, our analysis shows that these dynamics vanish with increasing number of tests (Monte-Carlo samplings). The reason is the disorder in the medium. For a persistent local stick-slip motion, for averaged tests, it would be necessary that the same grain-force-chain is placed (and broken) at the same position, at the same displacement. This might be true for small specimens, with few spheres which can get jammed or crystallized, but it becomes less probable for larger specimens, with larger geometric disorder. In a real fault, it would be even less likely to have exactly the same spatial arrangement along hundreds of meters, with the same composition and same properties. We thus

propose that the apparent friction is controlled by the global material behavior of gouges and not by the local chain breakages between particles.

The analysis has also shown that the material's critical slip distance, D_c, for the transition from peak to residual friction is comparable to the mean particle diameter of the sample. Scaling for maximum or minimum particle diameters did not show any sign of convergence to the obtained results. This is important as the polydispersity of gouge does not play such an important role for stability as much as the mean particle diameter. In the absence of very fine particles that can cause lubrication (Reches & Lockner, 2010), even for wide distributions as far as the fine content is not dominant (see Taha et al., 2019), d_{50} and its evolution seem to be a good descriptor for the gouge stability as used in Rattez, Stefanou, Sulem, Veveakis, et al. (2018), for example, without the need for an explicit description of the grain size distribution.

In all tests presented in this work, an important slip-weakening response is taking place (see e.g., Figure 7). The drop in friction is in all cases $\Delta\mu \simeq 0.3$ (see also Kanamori & Brodsky, 2004). In terms of stability, according to Section 2.2, the friction drop slope should be smaller than the system's stiffness, $-k$, for a stable, creep behavior to take place. Due to the very small critical slip distance in all cases (few d_{50}), the slope becomes too large to be sustained by a typical crust-rock ($G \simeq 30$ GPa) and L at meters scale. D_c in situ is found to be several orders of magnitude higher (see Byerlee, 1978; Kanamori & Brodsky, 2004). This difference can be attributed to various phenomena related to fault geometry, heterogeneity and multi-physical couplings, which our micro-mechanical model does not take into account. However, it provides useful insight in the micro-mechanisms that take place during seismic slip.

Of course, there is a number of assumptions in the present work and other additional mechanisms could explain differences between the results and in situ measurements. For example, Rabinowicz (1955) and Reches and Lockner (2010) have shown that small (particles product of wear) produced during shearing might lubricate the fault gouge and enhance slip-weakening behavior. Depending on which stage the lubrication-film is formed it might reduce the friction drop or enhance it. Given the high confinement of the seismogenic zone, grain breakage and ultra-cataclastic flow are also expected (Collins-Craft et al., 2020). In the present work, grain breakage is not simulated explicitly. However, an energy based analysis is derived (see Appendix A), showing that the released energy by particle-breakage is too little to affect the system's response. Thus, considering only the geometric entropy of the system, from the findings of this work, it is expected that a slow evolution of the fault gouge during shearing will widen the PSD (and thus will change the parameter f). The existence of few smaller fragments is not expected to affect the stability of the system. On the contrary, a fast evolution (reduction of the mean particle size, d_{50}) will reduce the critical slip distance, D_c, and thus will affect the stability. Further DEM simulations that include grain breakage (see e.g., Guo & Morgan, 2004) up to very fine particles might give more information in this aspect. Multi-scale simulations with state-of-the art tools such as TANN (Masi & Stefanou, 2022; Masi et al., 2021) could also provide insights. Other lubrication films may be created by multi-physical processes such as dehydration or melting of particles while self-healing might be present due to sintering (Reches & Lockner, 2010). These effects are expected to modify the apparent frictional properties of the gouge and should, therefore, be further investigated in future research. Furthermore, the complex interplay between competing multi-physical phenomena is found to have primary impact on fault's stability (Brantut & Sulem, 2012; Rattez, Stefanou, & Sulem, 2018; Rattez, Stefanou, Sulem, Veveakis, et al., 2018; Rempe et al., 2017; Stefanou & Sulem, 2016; Veveakis et al., 2010, 2013). All the above mechanisms are essential for grasping the frictional weakening of faults and they will be thus considered for future research.

6. Conclusions

In this work, we studied the apparent frictional behavior of a healed (but cohesion-less) fault gouge in seismogenic depth. The gouge material was simulated using the DEM and was assumed to be dry and in a highly interlocked initial state (as a result from cataclasis and long-term consolidation period). As a result, the material presented a strengthened initial state that leads to pronounced softening/weakening during slips. The results were interpreted in a stochastic way to account for the geometric disorder of gouge layers using Monte-Carlo analysis.

The main outcomes of this work are summarized below:

- Local stick-slip motion is found to statistically vanish for increasing number of (averaged) tests due to the geometric disorder of the granular medium. Moreover, the local stick-slips do not affect the expected value of the apparent frictional response.
- Both the thickness of the PSZ and the critical slip distance, D_c, are scaled with the mean particle diameter, d_{50}, and they are not significantly influenced by the PSD, f. Since DEM models are restricted to smaller domains due to the high computational cost, continuum methods are used for larger scale computations. The aforementioned finding is an important one, since it can justify the ad-hoc use of d_{50} as the main length scale in continuum models that take into account the size of the microstructure (e.g., Rattez, Stefanou, Sulem, Veveakis, et al., 2018).
- Shearing velocity seems to play secondary role under the conditions studied here. The consideration of Thermo-Hydro-Chemo-Mechanical (THCM) couplings at the level of the microstructure could lead to more important rate effects compared to the geometric entropy (complexity) that was only considered here.

Appendix A

Under the conditions met at the seismogenic zone (high confinement), grain crushing is expected during shearing. We showed that PSZ's width, λ, scales with the mean particle size, d_{50}, and so does the critical slip distance, D_c. The two properties D_c and λ did not show any scaling with particle size distribution. We thus consider the mean particle diameter, d_{50}, as the main descriptor of the gouge layer and particle crushing as the reduction of mean particle size, d_{50}. To account for grain-crushing, we model the evolution of the mean particle diameter assuming an exponential decrease of d_{50} with the total shear strain, γ_{12}, by Montési and Hirth (2003):

$$d_{50}(\gamma_{12}) = \left(d_{50_0} - d_{50}\right)e^{-\frac{\gamma_{12}}{\gamma_c}} + d_{50} \tag{A1}$$

where d_{50_0} is the mean particle diameter before grain crushing and d_{50} the final mean particle size. γ_c is a characteristic deformation that accounts for the rate of evolution, which will be here taken equal to 1 for simplicity. We show below the evolution of D_c and λ for $d_{50} \simeq 70\%$ and $d_{50} \simeq 50\%$ of the d_{50_0}.

Furthermore, we account for the energy density dissipated by grain crushing as follows. We consider the dissipated energy E_{gc} released during the crushing of a single grain to be:

$$E_{gc} = G_c A(d_{50}) = E_{gc}(d_{50}(\gamma_{12})) \tag{A2}$$

G_c is the surface energy associated to the material of the grain and A the created surface due to crushing. Consequently, the energy dissipation due to grain crushing for the transition from the first mean particle size, d_{50_0} to the current one d_{50}, is given by $\Delta E_{gc} = E_{gc} - E_{gc_0}$ or, more specifically, for the specimen:

$$\Delta E_{gc} = G_c N_p(d_{50}) \frac{\pi d_{50}^2}{2} = \frac{G_c}{2}\pi\left[N(d_{50})d_{50}^2 - N_p\left(d_{50_0}\right)d_{50_0}^2\right] \tag{A3}$$

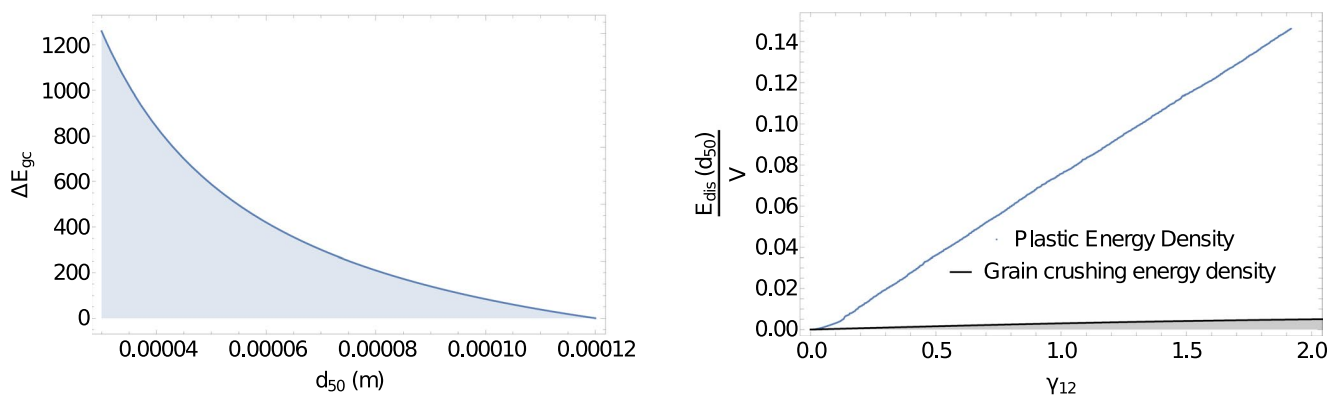

Figure A1. (left) Grain crushing energy for different mean particle sizes d_{50} and (right) energy densities for plastic dissipation and grain crushing.

where we use $G_c = 3 \times 10^{-3}$ (N/mm^2) which falls inside the values found in Wiederhorn (1969), $N_p = V(1-\xi)/\frac{4\pi d_{50}^2}{3}$ is the number of particles at the current state, with ξ being the porosity and V the total volume, which finally gives:

$$\Delta E_{gc} = \frac{3G_c}{8} V(1-\xi)\left(\frac{1}{d_{50}} - \frac{1}{d_{50_0}}\right) \tag{A4}$$

The lower bound on Figure A1 is closed by the findings of Stefanou and Sulem (2016). Comparing the energy dissipation densities of grain crushing and plastic dissipation for increasing plastic deformation, in Figure A1, one can observe that the final grain crushing energy corresponds to ∽4% of the plastic dissipation in the system and can thus be considered negligible.

Appendix B

Common laboratory experiments and DEM studies for the study of shearing behavior of fault gouges are based on sheared response of glass-beads. Glass-beads particles are easily modeled by spherical DEM and can thus provide a good source of experimental validation on numerical experiments. However, modeling gouge materials using glass-beads (and the related DEM numerical tests) for the study of fault gouges, disregards the initial state of the gouge. The gouge at seismogenic depth and inside the fault core is expected to be product of abrasive wear of the host rock and of ultra-cataclastic flow due to previous slip of the fault core. Thus, it is expected to be dense and highly interlocked.

As it is shown in Figure B1, disregarding the initial state of the granular material will lead to different gouge response under shear. For example, considering perfectly spherical, non-interlocked particles, the medium, will show a slip-strengthening behavior, thus no global friction drop at all. If rolling moments are present (to simulate angular particles), the response shows a slip-weakening behavior with a peak friction of $\mu_{peak} \sim 0.55$ and a friction drop of $\Delta\mu \sim 0.05$ following a very mild softening branch till the residual value. However, if the same particles are previously consolidated to a dense interlocked initial state, the response shows much higher friction coefficient of $\mu_{peak} \sim 0.8$ followed by a rather significant friction drop of $\Delta\mu \sim 0.3$ to the same residual value.

The maximum shear stress envelope for the studied material under different normal stress values after the initial consolidation (σ_c) is given in Figure B2. The numerical tests (represented by black dots) follow a parabolic envelope $\tau_{peak} = a\sigma_c^2 + b\sigma_c + c$, with $a = -0.0013$ (MPa^{-1}), $b = 1.0115$ (−), $c = 0.0$ (MPa) (blue line) and a coefficient of determination equal to $R^2 = 0.9998 \approx 1$. The same initial consolidated sample is used for every unloading case. The classical dependence of shear strength on normal stress in geomaterials is thus

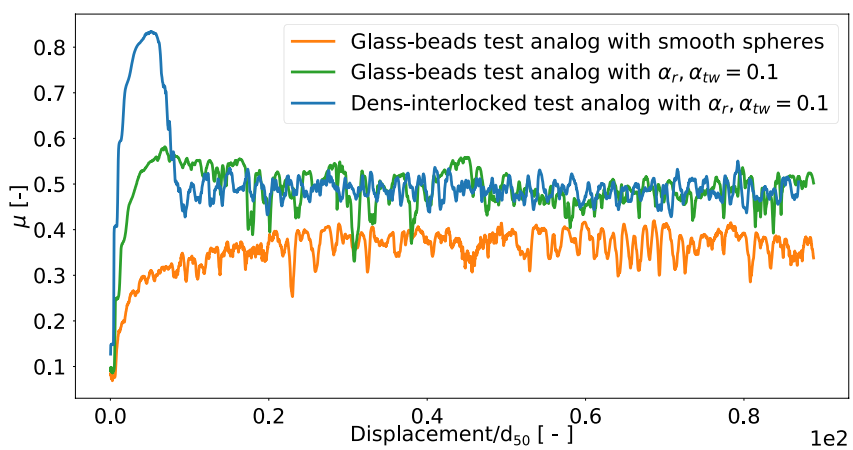

Figure B1. Effect of the initial conditions of the shearing test. In this plot, a shearing test that considers highly interlocked particles at the beginning of the test is compared to two tests where the material's consolidation is similar to glass-beads experiments.

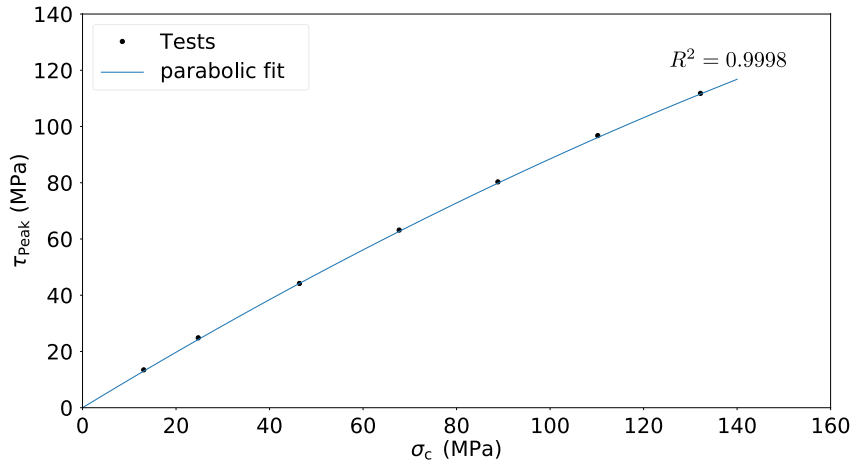

Figure B2. Maximum shear stress envelope for different normal loadings, after the initial consolidation.

captured and it reflects the effect of frictional cohesion-less ($c = 0$) interlocking (Goodman, 1989; Jaeger et al., 2009).

The derivative with respect to the normal stress represents the friction coefficient for a given normal stress. Notice, that many times in practice, the friction coefficient is informally given as the ratio of the shear stress over the normal stress (friction ratio) and it is not calculated using the above mentioned derivative. This can lead to inaccurate estimations of the friction coefficient, if the normal stress is varying (e.g., shearing under constant volume). However, in all the simulations presented herein, the normal stress was kept constant leading to non-isochoric shearing deformation. Thus, the dependence of the friction ratio in terms of the different parameters studied herein, represents the evolution of the friction coefficient at a specific normal stress. For other stresses a correction could be approximated by: $d\tau/d\sigma_c = d\mu/d\sigma_c\ \sigma_c + \mu$ (considering expressing τ as $\mu(\sigma_c)\sigma_c$.

The dilation of the numerical sample during shear is presented below. By definition the dilatancy, β, is equal to $\beta = \frac{\dot{\varepsilon}_v^{pl}}{\dot{\gamma}^{pl}}$, where $\dot{\varepsilon}_v^{pl}$ is the plastic volumetric strain rate and $\dot{\gamma}^{pl}$ is the shear plastic strain rate. Here, we calculated the average dilatancy of the sample after the peak, $\bar{\beta} = \frac{\bar{\varepsilon}_v^{pl}}{\bar{\gamma}^{pl}}$, where $\bar{\varepsilon}_v^{pl}$ is the average plastic volumetric strain and $\bar{\gamma}^{pl}$ is the average shear plastic strain after averaging at the post-peak shearing. The above quantity was calculated using the simulations of reference case (90*f*#0.0) and was found to be approximately equal to $\bar{\beta} \simeq 0.45°$. This dilatancy represents the dilation of the localized zone, as the parts of the specimen outside the shear band act almost as rigid bodies. Corrections for elastic strains were applied by fitting the elastic response at the beginning of shearing with a linear elastic model, but they were negligible.

The reported dilatancy is low, given the experience from laboratory experiments in soil mechanics. Our interpretation is that this is due to (a) high confining stresses in comparison with usual lab experiments of sands and (b) the fact that the calculated dilatancy represents the average dilation of the sample after the peak friction is met. Low values of dilation angles in faults are also reported and used in the literature (Sleep, 1999; Sleep et al., 2000).

Appendix C

Denoting the measured quantity of interest (here the critical slip distance D_c, the residual friction angle, μ_{res}, the peak friction angle, μ_{peak}, shear band thickness λ) of a trial "i" with y_i, the expected value, or else, the mean value of y is given by:

$$\mu_y \equiv E(y) = \int_{-\infty}^{\infty} y f(y) dy \tag{C1}$$

where $f(y)$ is the probability density of y.

For N number of tests, an estimator for μ_y would be:

$$\bar{y} = \frac{1}{N}\sum_{i=1}^{N} y_i \tag{C2}$$

Monte-Carlo involves random sampling of inputs, therefore different results (in terms of $\bar{y}$) are expected each time a probabilistic analysis is performed. The variance of the results of $\bar{y}$ varies from Monte-Carlo to Monte-Carlo simulation depends on the number of tests, N. Thus the accuracy of $\bar{y}$ is found by the expectation $\bar{y} - \mu_y$:

$$E(\bar{y} - \mu_y) = E(\bar{y}) - \mu_y = E\left(\frac{1}{N}\sum_{i=1}^{N} y_i\right) - \mu_y = \frac{1}{N}\sum_{i=1}^{N} E(y_i) - \mu_y \tag{C3}$$

Following Willcox and Wang (2014), since y_i occurs from random sampling of inputs when using Monte-Carlo, then $E(y_i) = \mu_y$. Thus $E(\bar{y} - \mu_y) = \frac{1}{N}N\mu_y - \mu_y = 0$. Hence, on average, the error in using $\bar{y}$ to approximate μ_y is zero and the estimator is unbiased. The variance $\mathrm{Var}(\bar{y} - \mu_y)$ can now be used to compute the variability of $\bar{y}$ (the variance of μ_y is zero since μ_y is a constant).

$$\mathrm{Var}(\bar{y} - \mu_y) = \frac{1}{N^2}\mathrm{Var}\left(\sum_{i=1}^{N} y_i\right) \tag{C4}$$

However, Monte-Carlo picks as input independent, random samples hence the variance of the sum of sample y_i is the sum of their variance:

$$\mathrm{Var}(\bar{y} - \mu_y) = \frac{\sigma_y^2}{N} \tag{C5}$$

The standard error of the estimator is finally given by: $\sigma_{\bar{y}} = \sigma_y/\sqrt{N}$.

Data Availability Statement

The generated numerical data presented in this study are publicly available in Zenodo repository (Papachristos et al., 2022).

Acknowledgments
This work was supported by the European Research Council (ERC) under the European Union Horizon 2020 research and innovation program (Grant 757848 Co-Quake).

References

Abe, S., Dieterich, J. H., Mora, P., & Place, D. (2002). Simulation of the influence of rate-and state-dependent friction on the macroscopic behavior of complex fault zones with the lattice solid model. *Pure and Applied Geophysics*, *159*(9), 1967–1983. https://doi.org/10.1007/s00024-002-8718-7

Abe, S., & Mair, K. (2009). Effects of gouge fragment shape on fault friction: New 3D modeling results. *Geophysical Research Letters*, *36*(23), L23302. https://doi.org/10.1029/2009gl040684

Aharonov, E., & Scholz, C. H. (2018). A physics-based rock friction constitutive law: Steady state friction. *Journal of Geophysical Research: Solid Earth*, *123*(2), 1591–1614. https://doi.org/10.1002/2016jb013829

Aharonov, E., & Sparks, D. (1999). Rigidity phase transition in granular packings. *Physical Review* E, *60*(6), 6890–6896. https://doi.org/10.1103/physreve.60.6890

Aharonov, E., & Sparks, D. (2002). Shear profiles and localization in simulations of granular materials. *Physical Review E*, *65*(5), 051302. https://doi.org/10.1103/physreve.65.051302

Anthony, J. L., & Marone, C. (2005). Influence of particle characteristics on granular friction. *Journal of Geophysical Research: Solid Earth*, *110*(B8), B08409. https://doi.org/10.1029/2004jb003399

Azéma, E., Estrada, N., & Radjai, F. (2012). Nonlinear effects of particle shape angularity in sheared granular media. *Physical Review E*, *86*(4), 041301. https://doi.org/10.1103/physreve.86.041301

Bak, P., Tang, C., & Wiesenfeld, K. (1988). Self-organized criticality. *Physical Review A*, *38*(1), 364–374. https://doi.org/10.1103/physreva.38.364

Beeler, N., Tullis, T., & Weeks, J. (1994). The roles of time and displacement in the evolution effect in rock friction. *Geophysical Research Letters*, *21*(18), 1987–1990. https://doi.org/10.1029/94gl01599

Ben-Zion, Y., & Sammis, C. G. (2003). Characterization of fault zones. *Pure and Applied Geophysics*, *160*(3), 677–715. https://doi.org/10.1007/pl00012554

Biegel, R. L., Sammis, C. G., & Dieterich, J. H. (1989). The frictional properties of a simulated gouge having a fractal particle distribution. *Journal of Structural Geology*, *11*(7), 827–846. https://doi.org/10.1016/0191-8141(89)90101-6

Blenkinsop, T. G. (1991). Cataclasis and processes of particle size reduction. *Pure and Applied Geophysics*, *136*(1), 59–86. https://doi.org/10.1007/bf00878888

Brantut, N., & Sulem, J. (2012). Strain localization and slip instability in a strain-rate hardening, chemically weakening material. *Journal of Applied Mechanics*, *79*(3), 031004. https://doi.org/10.1115/1.4005880
Brodie, K., Fettes, D., Harte, B., & Schmid, R. (2007). Structural terms including fault rock terms.
Byerlee, J. (1978). Friction of rocks. In *Rock friction and earthquake prediction* (pp. 615–626). Springer.
Cantor, D., Azéma, E., Sornay, P., & Radjai, F. (2018). Rheology and structure of polydisperse three-dimensional packings of spheres. *Physical Review E*, *98*(5), 052910. https://doi.org/10.1103/physreve.98.052910
Chambon, G., Schmittbuhl, J., & Corfdir, A. (2002). Laboratory gouge friction: Seismic-like slip-weakening and secondary rate-and state-effects. *Geophysical Research Letters*, *29*(10), 4–1. https://doi.org/10.1029/2001gl014467
Chester, F. M., & Chester, J. S. (1998). Ultracataclasite structure and friction processes of the Punchbowl fault, San Andrea system, California. *Tectonophysics*, *295*(1–2), 199–221. https://doi.org/10.1016/s0040-1951(98)00121-8
Collettini, C., Niemeijer, A., Viti, C., & Marone, C. (2009). Fault zone fabric and fault weakness. *Nature*, *462*(7275), 907–910. https://doi.org/10.1038/nature08585
Collins-Craft, N. A., Stefanou, I., Sulem, J., & Einav, I. (2020). A Cosserat Breakage Mechanics model for brittle granular media. *Journal of the Mechanics and Physics of Solids*, *55*(6), 103975. https://doi.org/10.1016/j.jmps.2020.103975
Davidesko, G., Sagy, A., & Hatzor, Y. H. (2014). Evolution of slip surface roughness through shear. *Geophysical Research Letters*, *41*(5), 1492–1498. https://doi.org/10.1002/2013gl058913
Dieterich, J. H. (1978). Time-dependent friction and the mechanics of stick-slip. In *Rock friction and earthquake prediction* (pp. 790–806). Springer.
Dieterich, J. H. (1979). Modeling of rock friction: 1. Experimental results and constitutive equations. *Journal of Geophysical Research: Solid Earth*, *84*(B5), 2161–2168. https://doi.org/10.1029/jb084ib05p02161
Dieterich, J. H., & Carter, N. (1981). Constitutive properties of faults with simulated gouge. Mechanical behavior of crustal rocks.
Dieterich, J. H., & Kilgore, B. D. (1994). Direct observation of frictional contacts: New insights for state-dependent properties. *Pure and Applied Geophysics*, *143*(1–3), 283–302. https://doi.org/10.1007/bf00874332
Dorostkar, O., Guyer, R. A., Johnson, P. A., Marone, C., & Carmeliet, J. (2017a). On the micromechanics of slip events in sheared, fluid-saturated fault gouge. *Geophysical Research Letters*, *44*(12), 6101–6108. https://doi.org/10.1002/2017gl073768
Dorostkar, O., Guyer, R. A., Johnson, P. A., Marone, C., & Carmeliet, J. (2017b). On the role of fluids in stick-slip dynamics of saturated granular fault gouge using a coupled computational fluid dynamics-discrete element approach. *Journal of Geophysical Research: Solid Earth*, *122*(5), 3689–3700. https://doi.org/10.1002/2017jb014099
Estrada, N., Azéma, E., Radjai, F., & Taboada, A. (2011). Identification of rolling resistance as a shape parameter in sheared granular media. *Physical Review E*, *84*(1), 011306. https://doi.org/10.1103/physreve.84.011306
Estrada, N., Taboada, A., & Radjai, F. (2008). Shear strength and force transmission in granular media with rolling resistance. *Physical Review E*, *78*(2), 021301. https://doi.org/10.1103/physreve.78.021301
Fairley, J., Heffner, J., & Hinds, J. (2003). Geostatistical evaluation of permeability in an active fault zone. *Geophysical Research Letters*, *30*(18). https://doi.org/10.1029/2003gl018064
Ferdowsi, B., Griffa, M., Guyer, R. A., Johnson, P. A., Marone, C., & Carmeliet, J. (2014). Three-dimensional discrete element modeling of triggered slip in sheared granular media. *Physical Review E*, *89*(4), 042204. https://doi.org/10.1103/physreve.89.042204
Ferdowsi, B., & Rubin, A. M. (2020). A granular-physics-based view of fault friction experiments. *Journal of Geophysical Research: Solid Earth*, *125*(6), e2019JB019016. https://doi.org/10.1029/2019jb019016
GDR MiDi (2004). On dense granular flows. *The European Physical Journal E*, *14*(4), 341–365. https://doi.org/10.1140/epje/i2003-10153-0
Goodman, R. E. (1989). *Introduction to rock mechanics* (Vol. 2). Wiley.
Gu, J.-C., Rice, J. R., Ruina, A. L., & Simon, T. T. (1984). Slip motion and stability of a single degree of freedom elastic system with rate and state dependent friction. *Journal of the Mechanics and Physics of Solids*, *32*(3), 167–196. https://doi.org/10.1016/0022-5096(84)90007-3
Guo, Y., & Morgan, J. K. (2004). Influence of normal stress and grain shape on granular friction: Results of discrete element simulations. *Journal of Geophysical Research: Solid Earth*, *109*(B12), B12305. https://doi.org/10.1029/2004jb003044
Guo, Y., & Morgan, J. K. (2006). The frictional and micromechanical effects of grain comminution in fault gouge from distinct element simulations. *Journal of Geophysical Research: Solid Earth*, *111*(B12). https://doi.org/10.1029/2005jb004049
Guo, Y., & Morgan, J. K. (2007). Fault gouge evolution and its dependence on normal stress and rock strength—Results of discrete element simulations: Gouge zone properties. *Journal of Geophysical Research: Solid Earth*, *112*(B10), B10403. https://doi.org/10.1029/2006jb004524
Hazzard, J. F., & Mair, K. (2003). The importance of the third dimension in granular shear. *Geophysical Research Letters, 30*(13). https://doi.org/10.1029/2003gl017534
Hooke, R. L., & Iverson, N. R. (1995). Grain size distribution in deforming subglacial tills: Role of grain fracture. *Geology*, *23*(1), 57–60. https://doi.org/10.1130/0091-7613(1995)023<0057:gsdids>2.3.co;2
Hosn, R. A., Sibille, L., Benahmed, N., & Chareyre, B. (2017). Discrete numerical modeling of loose soil with spherical particles and interparticle rolling friction. *Granular Matter*, *19*(1), 4. https://doi.org/10.1007/s10035-016-0687-0
Iwashita, K., & Oda, M. (1998). Rolling resistance at contacts in simulation of shear band development by DEM. *Journal of Engineering Mechanics*, *124*(3), 285–292. https://doi.org/10.1061/(asce)0733-9399(1998)124:3(285)
Jaeger, J. C., Cook, N. G., & Zimmerman, R. (2009). *Fundamentals of rock mechanics*. John Wiley & Sons.
Johnson, K. (1985). *Contact mechanics* (Vol. 95, p. 365). Cambridge University Press.
Kanamori, H., & Brodsky, E. E. (2004). The physics of earthquakes. *Reports on Progress in Physics*, *67*(8), 1429–1496. https://doi.org/10.1088/0034-4885/67/8/r03
Kawamoto, R., Andò, E., Viggiani, G., & Andrade, J. E. (2016). Level set discrete element method for three-dimensional computations with triaxial case study. *Journal of the Mechanics and Physics of Solids*, *91*, 1–13. https://doi.org/10.1016/j.jmps.2016.02.021
Koval, G., Roux, J.-N., Corfdir, A., & Chevoir, F. (2009). Annular shear of cohesionless granular materials: From the inertial to quasistatic regime. *Physical Review E*, *79*(2), 021306. https://doi.org/10.1103/physreve.79.021306
Kozicki, J., & Donzé, F. (2008). A new open-source software developed for numerical simulations using discrete modeling methods. *Computer Methods in Applied Mechanics and Engineering*, *197*(49–50), 4429–4443. https://doi.org/10.1016/j.cma.2008.05.023
Li, X. S., & Dafalias, Y. F. (2012). Anisotropic critical state theory: Role of fabric. *Journal of Engineering Mechanics*, *138*(3), 263–275. https://doi.org/10.1061/(asce)em.1943-7889.0000324
Liu, Y., Liu, H., & Mao, H. (2018). The influence of rolling resistance on the stress-dilatancy and fabric anisotropy of granular materials. *Granular Matter*, *20*(1), 12. https://doi.org/10.1007/s10035-017-0780-z
Lyakhovsky, V., & Ben-Zion, Y. (2014). A continuum damage-breakage faulting model and solid-granular transitions. *Pure and Applied Geophysics*, *171*(11), 3099–3123. https://doi.org/10.1007/s00024-014-0845-4

Lyakhovsky, V., Ben-Zion, Y., & Agnon, A. (1997). Distributed damage, faulting, and friction. *Journal of Geophysical Research: Solid Earth*, *102*(B12), 27635–27649. https://doi.org/10.1029/97jb01896

Mair, K., & Abe, S. (2008). 3D numerical simulations of fault gouge evolution during shear: Grain size reduction and strain localization. *Earth and Planetary Science Letters*, *274*(1–2), 72–81. https://doi.org/10.1016/j.epsl.2008.07.010

Mair, K., Frye, K. M., & Marone, C. (2002). Influence of grain characteristics on the friction of granular shear zones. *Journal of Geophysical Research: Solid Earth*, *107*(B10), ECV 4-1–ECV 4-9. https://doi.org/10.1029/2001jb000516

Mair, K., & Marone, C. (1999). Friction of simulated fault gouge for a wide range of velocities and normal stresses. *Journal of Geophysical Research: Solid Earth*, *104*(B12), 28899–28914. https://doi.org/10.1029/1999jb900279

Marone, C. (1998). Laboratory-derived friction laws and their application to seismic faulting. *Annual Review of Earth and Planetary Sciences*, *26*(1), 643–696. https://doi.org/10.1146/annurev.earth.26.1.643

Marone, C., Carpenter, B., & Schiffer, P. (2008). Transition from rolling to jamming in thin granular layers. *Physical Review Letters*, *101*(24), 248001. https://doi.org/10.1103/physrevlett.101.248001

Marone, C., Raleigh, C. B., & Scholz, C. (1990). Frictional behavior and constitutive modeling of simulated fault gouge. *Journal of Geophysical Research: Solid Earth*, *95*(B5), 7007–7025. https://doi.org/10.1029/jb095ib05p07007

Marone, C., & Scholz, C. (1989). Particle-size distribution and microstructures within simulated fault gouge. *Journal of Structural Geology*, *11*(7), 799–814. https://doi.org/10.1016/0191-8141(89)90099-0

Masi, F., & Stefanou, I. (2022). Multiscale modeling of inelastic materials with Thermodynamics-based Artificial Neural Networks (TANN). *Computer Methods in Applied Mechanics and Engineering*, *398*, 115190. https://doi.org/10.1016/j.cma.2022.115190

Masi, F., Stefanou, I., Vannucci, P., & Maffi-Berthier, V. (2021). Thermodynamics-based artificial neural networks for constitutive modeling. *Journal of the Mechanics and Physics of Solids*, *147*, 104277. https://doi.org/10.1016/j.jmps.2020.104277

Mollon, G., Quacquarelli, A., Andò, E., & Viggiani, G. (2020). Can friction replace roughness in the numerical simulation of granular materials? *Granular Matter*, *22*(2), 1–16. https://doi.org/10.1007/s10035-020-1004-5

Montési, L. G., & Hirth, G. (2003). Grain size evolution and the rheology of ductile shear zones: From laboratory experiments to postseismic creep. *Earth and Planetary Science Letters*, *211*(1–2), 97–110. https://doi.org/10.1016/s0012-821x(03)00196-1

Morgan, J. K. (1999). Numerical simulations of granular shear zones using the distinct element method: 2. Effects of particle size distribution and interparticle friction on mechanical behavior. *Journal of Geophysical Research: Solid Earth*, *104*(B2), 2721–2732. https://doi.org/10.1029/1998jb900055

Morgan, J. K. (2004). Particle dynamics simulations of rate-and state-dependent frictional sliding of granular fault gouge. In *Computational earthquake science part I* (pp. 1877–1891). Springer.

Morgan, J. K., & Boettcher, M. S. (1999). Numerical simulations of granular shear zones using the distinct element method: 1. Shear zone kinematics and the micromechanics of localization. *Journal of Geophysical Research: Solid Earth*, *104*(B2), 2703–2719. https://doi.org/10.1029/1998jb900056

Morrow, C., Shi, L., & Byerlee, J. (1984). Permeability of fault gouge under confining pressure and shear stress. *Journal of Geophysical Research: Solid Earth*, *89*(B5), 3193–3200. https://doi.org/10.1029/jb089ib05p03193

Mühlhaus, H.-B., & Vardoulakis, I. (1987). The thickness of shear bands in granular materials. *Géotechnique*, *37*(3), 271–283. https://doi.org/10.1680/geot.1987.37.3.271

Needleman, A. (1988). Material rate dependence and mesh sensitivity in localization problems. *Computer Methods in Applied Mechanics and Engineering*, *67*(1), 69–85. https://doi.org/10.1016/0045-7825(88)90069-2

Nguyen, D.-H., Azéma, E., Sornay, P., & Radjai, F. (2015). Effects of shape and size polydispersity on strength properties of granular materials. *Physical Review E*, *91*(3), 032203. https://doi.org/10.1103/physreve.91.032203

Numelin, T., Marone, C., & Kirby, E. (2007). Frictional properties of natural fault gouge from a low-angle normal fault, Panamint valley, California. *Tectonics*, *26*(2). https://doi.org/10.1029/2005tc001916

Ostoja-Starzewski, M. (2006). Material spatial randomness: From statistical to representative volume element. *Probabilistic Engineering Mechanics*, *21*(2), 112–132. https://doi.org/10.1016/j.probengmech.2005.07.007

Papachristos, E., & Stefanou, I. (2021). Controlling earthquake-like instabilities using artificial intelligence. arXiv preprint arXiv:2104.13180.

Papachristos, E., Stefanou, I., & Sulem, J. (2022). A discrete elements study of the frictional behavior of fault gouges: Numerical data. Zenodo. https://doi.org/10.5281/zenodo.6869242

Plassiard, J.-P., Belheine, N., & Donzé, F.-V. (2009). A spherical discrete element model: Calibration procedure and incremental response. *Granular Matter*, *11*(5), 293–306. https://doi.org/10.1007/s10035-009-0130-x

Platt, J. D., Rudnicki, J. W., & Rice, J. R. (2014). Stability and localization of rapid shear in fluid-saturated fault gouge: 2. Localized zone width and strength evolution. *Journal of Geophysical Research: Solid Earth*, *119*(5), 4334–4359. https://doi.org/10.1002/2013jb010711

Rabinowicz, E. (1951). The nature of the static and kinetic coefficients of friction. *Journal of Applied Physics*, *22*(11), 1373–1379. https://doi.org/10.1063/1.1699869

Rabinowicz, E. (1955). The relation between friction and wear for boundary-lubricated surfaces. *Proceedings of the Physical Society Section B*, *68*(9), 603–608. https://doi.org/10.1088/0370-1301/68/9/304

Rabinowicz, E. (1958). The intrinsic variables affecting the stick-slip process. *Proceedings of the Physical Society*, *71*(4), 668–675. https://doi.org/10.1088/0370-1328/71/4/316

Radjaï, F., & Dubois, F. (2011). *Discrete-element modeling of granular materials*. Wiley-ISTE.

Rattez, H., Stefanou, I., & Sulem, J. (2018a). The importance of thermo-hydro-mechanical couplings and microstructure to strain localization in 3D continua with application to seismic faults. Part I: Theory and linear stability analysis. *Journal of the Mechanics and Physics of Solids*, *115*, 54–76. https://doi.org/10.1016/j.jmps.2018.03.004

Rattez, H., Stefanou, I., Sulem, J., Veveakis, M., & Poulet, T. (2018b). The importance of thermo-hydro-mechanical couplings and microstructure to strain localization in 3D continua with application to seismic faults. Part II: Numerical implementation and post-bifurcation analysis. *Journal of the Mechanics and Physics of Solids*, *115*, 1–29. https://doi.org/10.1016/j.jmps.2018.03.003

Reches, Z., & Lockner, D. A. (2010). Fault weakening and earthquake instability by powder lubrication. *Nature*, *467*(7314), 452–455. https://doi.org/10.1038/nature09348

Rempe, M., Smith, S., Mitchell, T., Hirose, T., & Di Toro, G. (2017). The effect of water on strain localization in calcite fault gouge sheared at seismic slip rates. *Journal of Structural Geology*, *97*, 104–117. https://doi.org/10.1016/j.jsg.2017.02.007

Rice, J., & Ruina, A. L. (1983). Stability of steady frictional slipping. *Journal of Applied Mechanics*, *50*(2), 343–349. https://doi.org/10.1115/1.3167042

Rice, J. R. (1976). *Localization of plastic deformation (Technical Report)*. Brown University.

Rice, J. R. (1993). Spatio-temporal complexity of slip on a fault. *Journal of Geophysical Research: Solid Earth*, *98*(B6), 9885–9907. https://doi.org/10.1029/93jb00191

Rognon, P. G., Roux, J.-N., Naaim, M., & Chevoir, F. (2008). Dense flows of cohesive granular materials. *Journal of Fluid Mechanics*, *596*, 21–47. https://doi.org/10.1017/s0022112007009329

Rognon, P. G., Roux, J.-N., Wolf, D., Naaïm, M., & Chevoir, F. (2006). Rheophysics of cohesive granular materials. *Europhysics Letters*, *74*(4), 644–650. https://doi.org/10.1209/epl/i2005-10578-y

Rudnicki, J. W., & Rice, J. (1975). Conditions for the localization of deformation in pressure-sensitive dilatant materials. *Journal of the Mechanics and Physics of Solids*, *23*(6), 371–394. https://doi.org/10.1016/0022-5096(75)90001-0

Ruina, A. (1983). Slip instability and state variable friction laws. *Journal of Geophysical Research: Solid Earth*, *88*(B12), 10359–10370. https://doi.org/10.1029/jb088ib12p10359

Saffer, D. M., & Marone, C. (2003). Comparison of smectite-and illite-rich gouge frictional properties: Application to the updip limit of the seismogenic zone along subduction megathrusts. *Earth and Planetary Science Letters*, *215*(1–2), 219–235. https://doi.org/10.1016/s0012-821x(03)00424-2

Sammis, C., King, G., & Biegel, R. (1987). The kinematics of gouge deformation. *Pure and Applied Geophysics*, *125*(5), 777–812. https://doi.org/10.1007/bf00878033

Sammis, C. G., & Ben-Zion, Y. (2008). Mechanics of grain- size reduction in fault zones. *Journal of Geophysical Research: Solid Earth*, *113*(B2), B02306. https://doi.org/10.1029/2006jb004892

Sammis, C. G., Osborne, R. H., Anderson, J. L., Banerdt, M., & White, P. (1986). Self-similar cataclasis in the formation of fault gouge. *Pure and Applied Geophysics*, *124*(1–2), 53–78. https://doi.org/10.1007/bf00875719

Scholz, C. H. (2002). *The mechanics of earthquakes and faulting*. Cambridge University Press.

Scuderi, M. M., & Collettini, C. (2016). The role of fluid pressure in induced versus triggered seismicity: Insights from rock deformation experiments on carbonates. *Scientific Reports*, *6*(1), 24852. https://doi.org/10.1038/srep24852

Scuderi, M. M., Collettini, C., & Marone, C. (2017). Frictional stability and earthquake triggering during fluid pressure stimulation of an experimental fault. *Earth and Planetary Science Letters*, *477*, 84–96. https://doi.org/10.1016/j.epsl.2017.08.009

Shire, T., Hanley, K. J., & Stratford, K. (2021). Dem simulations of polydisperse media: Efficient contact detection applied to investigate the quasi-static limit. *Computational Particle Mechanics*, *8*(4), 653–663. https://doi.org/10.1007/s40571-020-00361-2

Sibson, R. H. (2011). The scope of earthquake geology. *Geological Society, London, Special Publications*, *359*(1), 319–331. https://doi.org/10.1144/sp359.18

Sleep, N. H. (1999). Rate-and state-dependent friction of intact rock and gouge. *Journal of Geophysical Research: Solid Earth*, *104*(B8), 17847–17855. https://doi.org/10.1029/1999jb900185

Sleep, N. H., Richardson, E., & Marone, C. (2000). Physics of friction and strain rate localization in synthetic fault gouge. *Journal of Geophysical Research: Solid Earth*, *105*(B11), 25875–25890. https://doi.org/10.1029/2000jb900288

Šmilauer, V., Angelidakis, V., Catalano, E., Caulk, R., Chareyre, B., Chèvremont, W., et al. (2021). *Yade Documentation* (3rd ed.). The Yade Project. https://doi.org/10.5281/zenodo.5705394

Šmilauer, V., Catalano, E., Chareyre, B., Dorofeenko, S., Duriez, J., Dyck, N., et al. (2015). Reference manual. In *Yade documentation* (2nd ed.). The Yade Project. https://doi.org/10.5281/zenodo.34045

Stefanou, I. (2019). Controlling anthropogenic and natural seismicity: Insights from active stabilization of the spring-slider model. *Journal of Geophysical Research: Solid Earth*, *124*(8), 8786–8802. https://doi.org/10.1029/2019JB017847

Stefanou, I., & Sulem, J. (2016). Existence of a threshold for brittle grains crushing strength: Two-versus three-parameter Weibull distribution fitting. *Granular Matter*, *18*(2), 14. https://doi.org/10.1007/s10035-015-0603-z

Stefanou, I., & Tzortzopoulos, G. (2022). Preventing instabilities and inducing controlled, slow-slip in frictionally unstable systems. *Journal of Geophysical Research: Solid Earth*, *127*, e2021JB023410. https://doi.org/10.1029/2021JB023410

Sulem, J., & Famin, V. (2009). Thermal decomposition of carbonates in fault zones: Slip-weakening and temperature-limiting effects. *Journal of Geophysical Research: Solid Earth*, *114*(B3), B03309. https://doi.org/10.1029/2008jb006004

Taha, H., Nguyen, N.-S., Marot, D., Hijazi, A., & Abou-Saleh, K. (2019). Micro-scale investigation of the role of finer grains in the behavior of bidisperse granular materials. *Granular Matter*, *21*(2), 28. https://doi.org/10.1007/s10035-019-0867-9

Takahashi, M. (2003). Permeability change during experimental fault smearing. *Journal of Geophysical Research: Solid Earth*, *108*(B5). https://doi.org/10.1029/2002jb001984

Tinti, E., Scuderi, M. M., Scognamiglio, L., Di Stefano, G., Marone, C., & Collettini, C. (2016). On the evolution of elastic properties during laboratory stick-slip experiments spanning the transition from slow slip to dynamic rupture. *Journal of Geophysical Research: Solid Earth*, *121*(12), 8569–8594. https://doi.org/10.1002/2016JB013545

Tzortzopoulos, G., Braun, P., & Stefanou, I. (2021). Absorbent porous paper reveals how earthquakes could be mitigated. *Geophysical Research Letters*, *48*(3), e2020GL090792. https://doi.org/10.1029/2020gl090792

Verberne, B. A., van den Ende, M., Chen, J., Niemeijer, A. R., & Spiers, C. J. (2020). The physics of fault friction: Insights from experiments on simulated gouges at low shearing velocities. *Solid Earth*, *11*(6), 2075–2095. https://doi.org/10.5194/se-11-2075-2020

Veveakis, M., Alevizos, S., & Vardoulakis, I. (2010). Chemical reaction capping of thermal instabilities during shear of frictional faults. *Journal of the Mechanics and Physics of Solids*, *58*(9), 1175–1194. https://doi.org/10.1016/j.jmps.2010.06.010

Veveakis, M., Stefanou, I., & Sulem, J. (2013). Failure in shear bands for granular materials: Thermo-hydro-chemo-mechanical effects. *Géotechnique Letters*, *3*, 31–36. https://doi.org/10.1680/geolett.12.00063[

Voivret, C., Radjai, F., Delenne, J.-Y., & El Youssoufi, M. S. (2009). Multiscale force networks in highly polydisperse granular media. *Physical Review Letters*, *102*(17), 178001. https://doi.org/10.1103/physrevlett.102.178001

Wang, C., Elsworth, D., & Fang, Y. (2019). Ensemble shear strength, stability, and permeability of mixed mineralogy fault gouge recovered from 3D granular models. *Journal of Geophysical Research: Solid Earth*, *124*(1), 425–441. https://doi.org/10.1029/2018jb016066

Wang, W., & Scholz, C. H. (1994). Wear processes during frictional sliding of rock: A theoretical and experimental study. *Journal of Geophysical Research: Solid Earth*, *99*(B4), 6789–6799. https://doi.org/10.1029/93jb02875

Wiederhorn, S. M. (1969). Fracture surface energy of glass. *Journal of the American Ceramic Society*, *52*(2), 99–105. https://doi.org/10.1111/j.1151-2916.1969.tb13350.x

Willcox, K., & Wang, Q. (2014). *16.90 computational methods in aerospace engineering*. Massachusetts Institute of Technology: MIT OpenCourseWare, Spring 2014.

Wood, D. M. (1990). *Soil behavior and critical state soil mechanics*. Cambridge University Press.